Electronic Supplementary Information (ESI)

Synthesis of stretchable triboelectric material with strain-compensating ability using gradient interpenetrating polymer networks

Do-Wan Kim,[a][‡] Hyeonwoo Mun,[b][‡] Yeonghun Kang,[b] Weon-Guk Kim,[a] Dahye Ahn,[b] Seong-Yun Yun,[a] Jeong-A Han,[a] Do Hoon Lee,[a] Taegoon Lee,[a] Kihoon Jeong,[b] Jihan Kim,[b] Sung Gap Im,*[b] and Yang-Kyu Choi*[a]

[a] School of Electrical Engineering

Korea Advanced Institute of Science and Technology (KAIST)

291 Daehak-ro, Yuseong-gu, Daejeon 34141, Republic of Korea

* E-mail: ykchoi@ee.kaist.ac.kr

[b] Department of Chemical and Biomolecular Engineering

Korea Advanced Institute of Science and Technology (KAIST)

291 Daehak-ro, Yuseong-gu, Daejeon 34141, Republic of Korea

* E-mail: sgim@kaist.ac.kr

‡ These authors contributed equally to this work.

Contents

under stretched ($\varepsilon = 100\%$) state for $t_{IPN,equiv}$ of 25 nm or less.

Supplementary Figure S21: OM images of Ecoflex-CNT with g-IPN under unstretched ($\varepsilon = 0\%$) and stretched ($\varepsilon = 100\%$) states for various $t_{IPN,equiv}$.

Supplementary Figure S22: AFM topography images of Ecoflex-CNT with g-IPN under unstretched ($\varepsilon = 0\%$) and stretched ($\varepsilon = 100\%$) states for various $t_{IPN,equiv}$.

Supplementary Figure S23: Simple analytical model describing the increase in surface area of the Ecoflex-CNT with g-IPN ($t_{IPN,equiv} = 75$ nm) under increasing strain.

Supplementary Figure S24: Measured R_s of pure Ecoflex-CNT and Ecoflex-CNT with g-IPN ($t_{IPN,equiv} = 75$ nm) under various strains.

Supplementary Figure S25: OM images and residual strain of Ecoflex-CNT with g-IPN ($t_{IPN,equiv} = 75$ nm), released after various iterative stretching ($\varepsilon = 100\%$) and releasing cycles.

Supplementary Figure S26: Fabrication process of the 3D-TENG and 3D-IPN-TENG.

Supplementary Figure S27: Measured pore diameter of Ecoflex-CNT sponges with and without g-IPN.

Supplementary Figure S28: Compressive stress-strain curves for Ecoflex-CNT sponges with and without g-IPN.

Supplementary Figure S29: Theoretical and experimental optimization of pore diameter for the sponge-structured 3D elastic TENGs.

Supplementary Figure S30: FEM simulation of the compression of Ecoflex-CNT sponge with g-IPN.

Supplementary Figure S31: Comparison of average power density between the 3D-TENG and 3D-IPN-TENG.

Supplementary Figure S32: Comparison of V_{cap} between a PMC composed of a full-wave rectifier and a buck converter and one with only a full-wave rectifier.

Supplementary Table S1: Systematic comparison of output performance and mechanical properties with previous works on stretchable TENGs.

Supplementary Table S2: Systematic comparison of output performance between 2D-IPN-TENG and 3D-IPN-TENG.

Supplementary Note S1: Tape peeling experiment and subsequent ToF-SIMS analyses.

Supplementary Note S2: Bulk mechanical and triboelectric properties of the uniform IPN (Case III).

Supplementary Note S3: The demonstration of synergistic performance enhancement in Ecoflex-CNT with g-IPN synthesized using guest polymers other than pVP.

Supplementary Note S4: Theoretical calculation process of RCA.

Supplementary Note S5: A simple analytical model describing the increase in surface area of the Ecoflex-CNT with g-IPN ($t_{IPN,equiv} = 75$ nm) under increasing strain.

Supplementary Note S6: Theoretical and experimental optimization of pore diameter for the

sponge-structured 3D elastic TENGs.

Supplementary References: 1-36.

Supplementary Movie S1: Simultaneously driving a stopwatch and a thermohygrometer by a 3D-IPN-TENG.
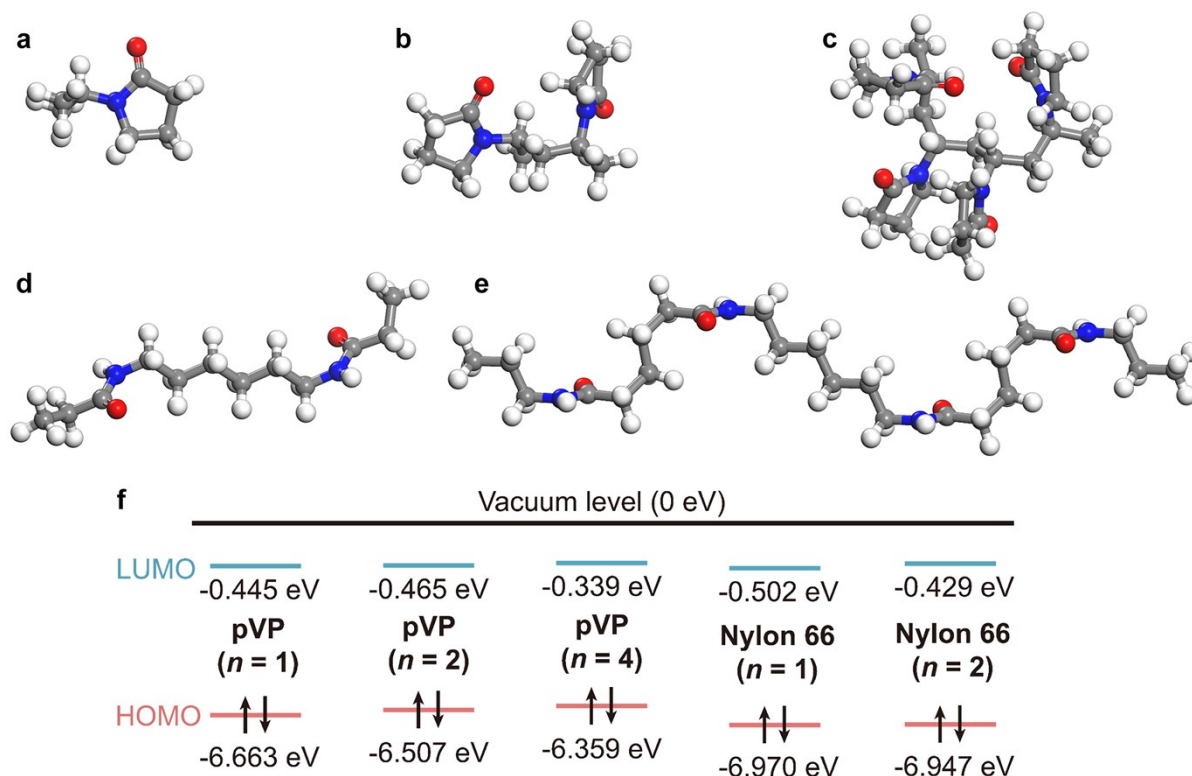
Figure S1. DFT calculation results for various chain lengths of pVP and Nylon 66. The molecular structures of (a) a pVP monomer, (b) a pVP dimer, (c) a pVP tetramer, (d) a Nylon 66 monomer, and (e) a Nylon 66 dimer used in the DFT calculations are shown. Grey, red, blue, and white represent carbon, oxygen, nitrogen, and hydrogen atoms, respectively. (f) The energy band diagram of pVP and Nylon 66 with various chain lengths obtained from DFT calculations. *n* denotes the chain length. For all cases, electron donation from pVP to Nylon 66 was more favorable than electron donation from Nylon 66 to pVP.
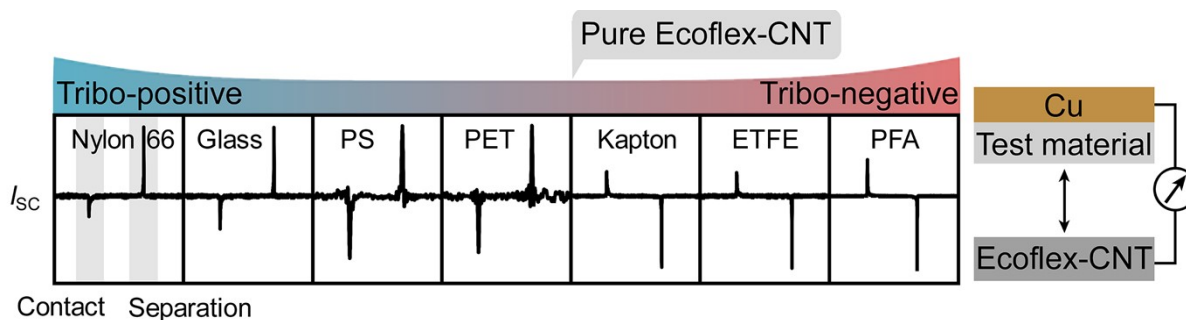
Figure S2. Measured I_{SC} showing the relative position of the pure Ecoflex-CNT in the triboelectric series. The resulting waveforms of the I_{SC} show that the relative position of pure Ecoflex-CNT in the triboelectric series was between polyethylene terephthalate (PET) and Kapton.
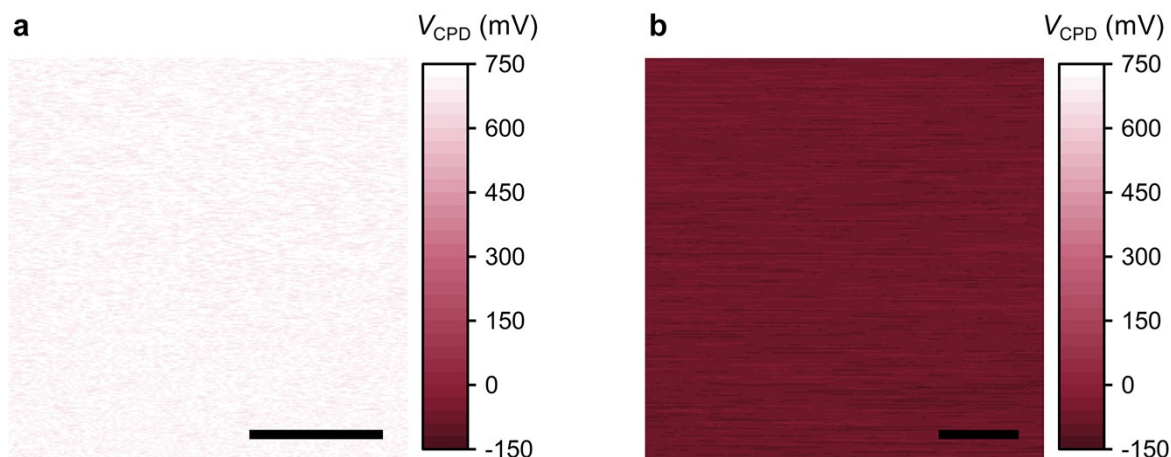
Figure S3. Kelvin probe force microscopy (KPFM) images of pure pVP and pure Ecoflex-CNT. (a) KPFM image of pure pVP. The mean V_{CPD} was 715.1 mV. (b) KPFM image of pure Ecoflex-CNT. The mean V_{CPD} was -72.1 mV. For (a) and (b), scale bars are 1 μm. Note that a higher V_{CPD} indicates a lower work function.[1]
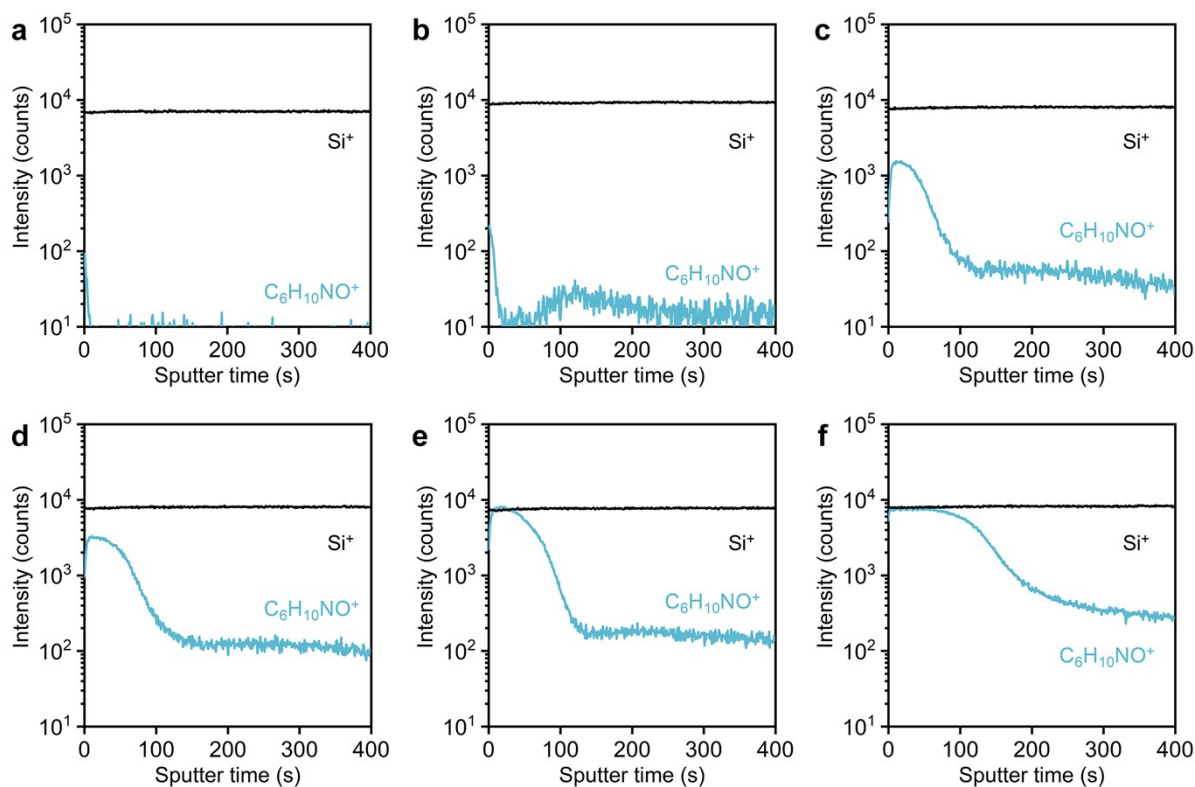
Figure S4. ToF-SIMS depth profiles of Ecoflex-CNT with g-IPN for various $t_{IPN,equiv}$. ToF-SIMS depth profiles of Ecoflex-CNT with g-IPN, obtained at $t_{IPN,equiv}$ of (a) 5 nm, (b) 10 nm, (c) 100 nm, (d) 150 nm, (e) 300 nm, and (f) 500 nm, are shown.
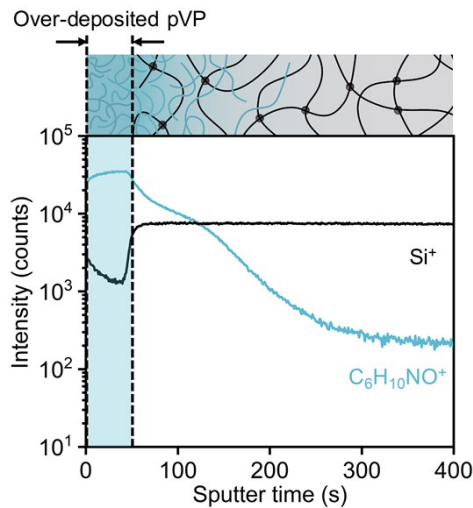
Figure S5. ToF-SIMS depth profile of over-deposited Ecoflex-CNT ($t_{\text{IPN,equiv}}$ = 1000 nm). The ToF-SIMS depth profile of the over-deposited Ecoflex-CNT shows that an unintended additional top layer of pure pVP was formed over the g-IPN.
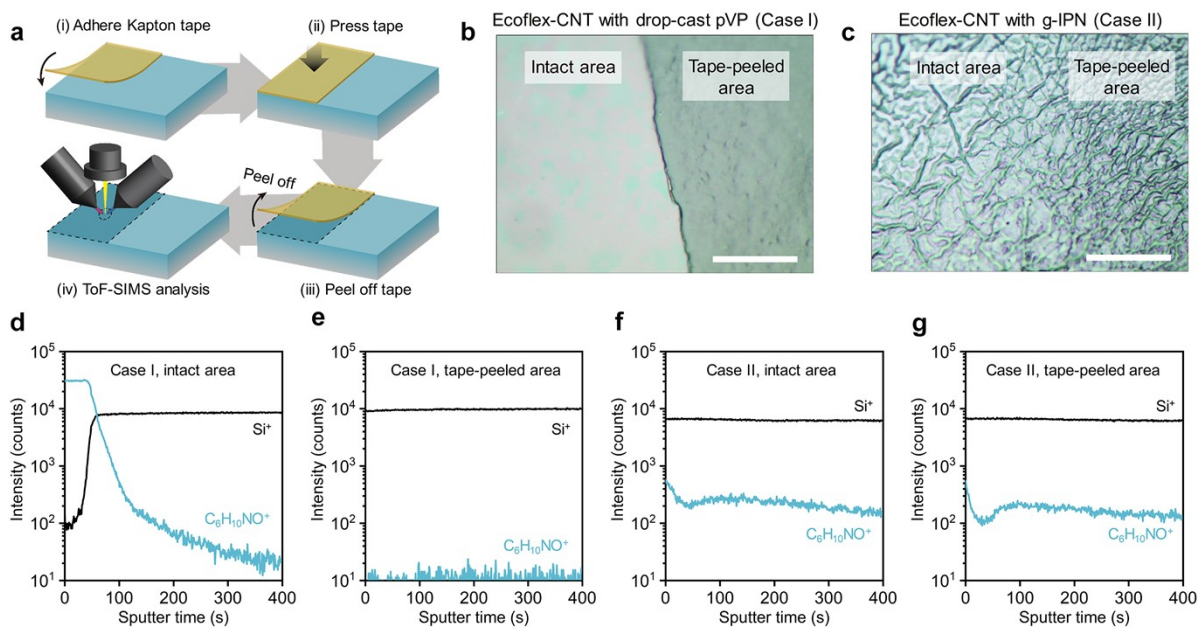
Figure S6. Tape peeling experiment and subsequent ToF-SIMS analyses. (a) Experimental procedure for the tape peeling experiment and subsequent ToF-SIMS analyses. (b) OM image of the intact area and tape-peeled area in Case I (Ecoflex-CNT with drop-cast pVP). (c) OM image of the intact area and tape-peeled area in Case II (Ecoflex-CNT with g-IPN, $t_{\text{IPN,equiv}}$ = 75 nm). Scale bars in (b) and (c) are 50 μm. (d) ToF-SIMS depth profile in Case I, obtained from the intact area. (e) ToF-SIMS depth profile in Case I, obtained from the tape-peeled area. (f) ToF-SIMS depth profile in Case II, obtained from the intact area. (g) ToF-SIMS depth profile in Case II, obtained from the tape-peeled area. For (f) and (g), $t_{\text{IPN,equiv}}$ was 75 nm.
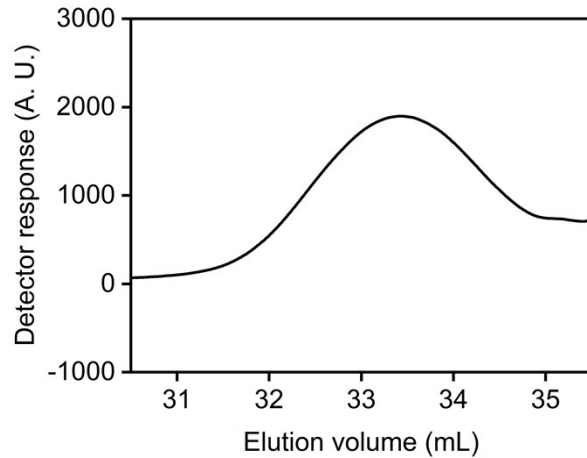
Figure S7. Gel permeation chromatography (GPC) measurement result of the iCVD-synthesized pVP.
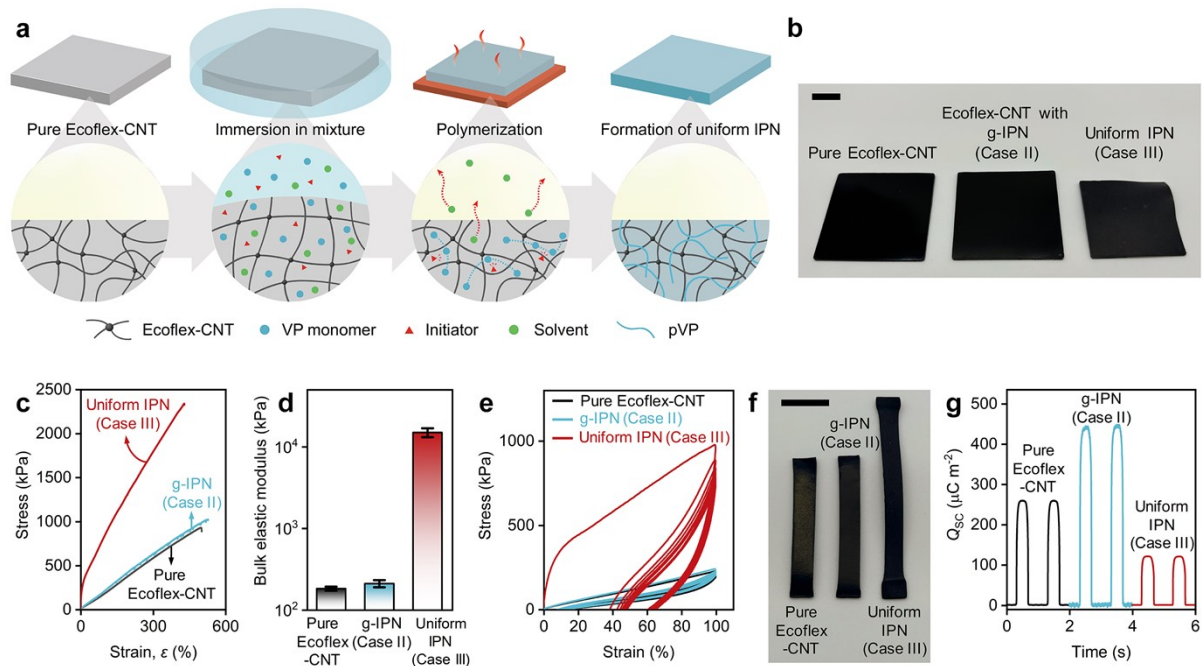
Figure S8. Synthesis procedure and bulk mechanical and triboelectric properties of the uniform IPN (Case III). (a) Synthesis procedure for the samples for Case III. (b) Photograph of the as-prepared samples of pure Ecoflex-CNT, Case II, and Case III. (c) Comparison of the stress-strain curves for pure Ecoflex-CNT, Case II, and Case III. (d) Comparison of the bulk elastic modulus of pure Ecoflex-CNT, Case II, and Case III. (e) Stress-strain curves of pure Ecoflex-CNT, Case II, and Case III during 10 iterative stretching ($\varepsilon = 100\%$) and releasing cycles. (f) Photograph of the samples of pure Ecoflex-CNT, Case II, and Case III released after stretching ($\varepsilon = 100\%$). Although the initial lengths of the samples were the same, Case III exhibited significantly higher residual strain compared to that of pure Ecoflex-CNT and Case II. (g) Measured Q_{SC} for pure Ecoflex-CNT, Case II, and Case III. Scale bars in (b) and (f) are 1 cm. For (b)-(g), $t_{IPN,equiv}$ of Case II was 75 nm.

Figure S9. Demonstration of synergistic performance enhancement in Ecoflex-CNT with g-IPN synthesized using pVI. (a) Chemical structures of 1-vinylimidazole and poly(1-vinylimidazole) (pVI). pVI was synthesized by free-radical polymerization using TBPO as the initiator. (b) Measured I_{SC} showing the relative position of pVI in the triboelectric series (left) and a simplified cross-sectional schematic of the measurement for identifying the relative position in the triboelectric series (right). The thickness of the pure pVI film used in this experiment was 3 μm. (c) ToF-SIMS depth profile of pure Ecoflex-CNT ($t_{\text{IPN,equiv}} = 0$ nm). (d) ToF-SIMS depth profile of Ecoflex-CNT with g-IPN synthesized using pVI ($t_{\text{IPN,equiv}} = 75$ nm). (e) OM image of Ecoflex-CNT with g-IPN synthesized using pVI ($t_{\text{IPN,equiv}} = 75$ nm) prior to applying strain, along with its schematic illustration (left). OM image of Ecoflex-CNT with g-IPN synthesized using pVI ($t_{\text{IPN,equiv}} = 75$ nm) released after applying 100% strain, along with its schematic illustration (right). Scale bars in (e) are 50 μm. (f) Photographs of the counter-contacting layers and the bottom layers used to evaluate triboelectric properties. (g) Measured Q_{SC} and V_{OC} for Ecoflex-CNT with g-IPN synthesized using pVI ($t_{\text{IPN,equiv}} = 75$ nm) and its control groups, using various counter-contacting materials.
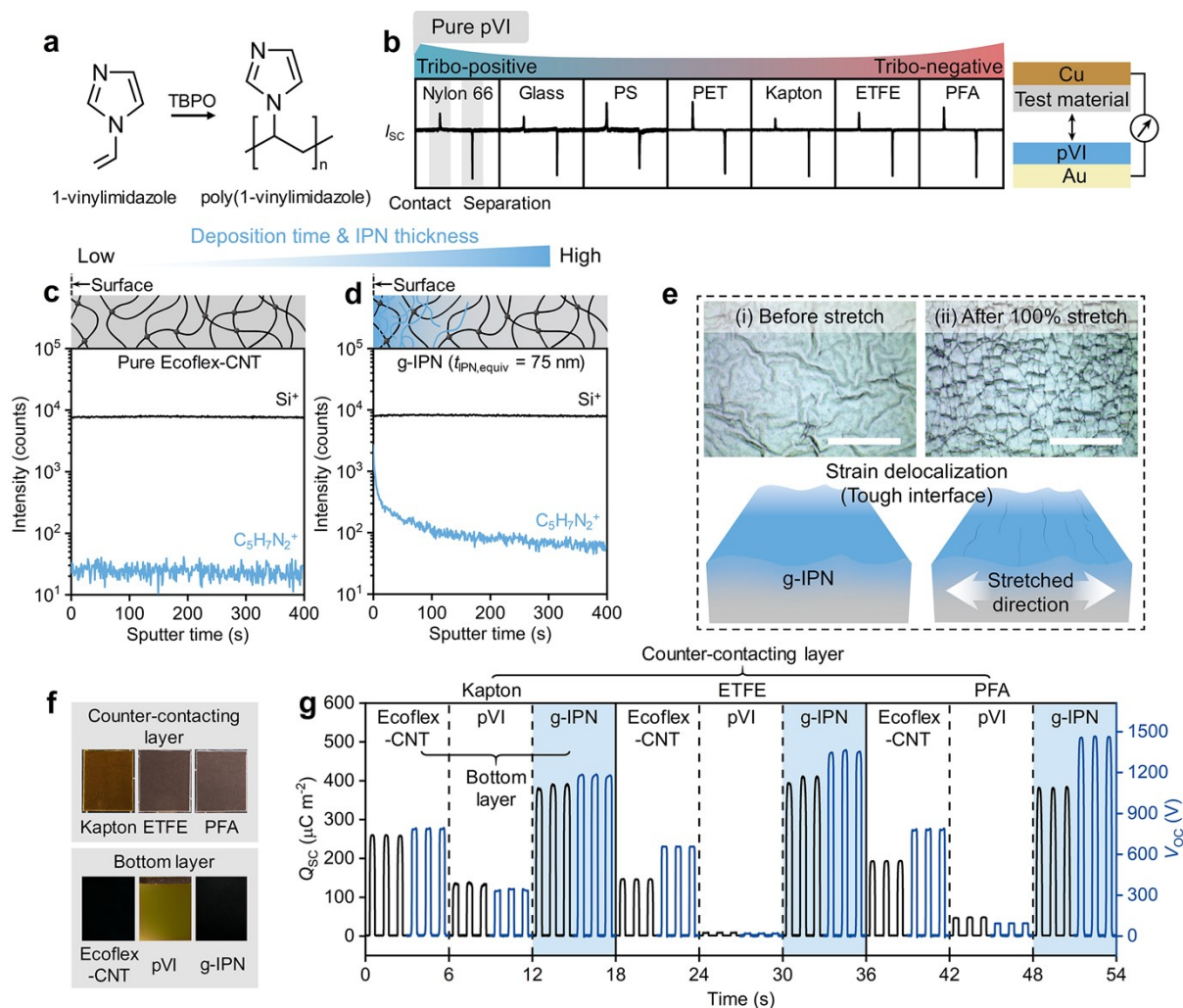
Figure S10. Demonstration of synergistic performance enhancement in Ecoflex-CNT with g-IPN synthesized using pAA. (a) Chemical structures of acrylic acid and poly(acrylic acid) (pAA). pAA was synthesized by free-radical polymerization using TBPO as the initiator. (b) Measured I_{SC} showing the relative position of pAA in the triboelectric series (left) and a simplified cross-sectional schematic of the measurement for identifying the relative position in the triboelectric series (right). The thickness of the pure pAA film used in this experiment was 3 μm. (c) ToF-SIMS depth profile of pure Ecoflex-CNT ($t_{IPN,equiv}$ = 0 nm). (d) ToF-SIMS depth profile of Ecoflex-CNT with g-IPN synthesized using pAA ($t_{IPN,equiv}$ = 75 nm). (e) OM image of Ecoflex-CNT with g-IPN synthesized using pAA ($t_{IPN,equiv}$ = 75 nm) prior to applying strain, along with its schematic illustration (left). OM image of Ecoflex-CNT with g-IPN synthesized using pAA ($t_{IPN,equiv}$ = 75 nm) released after applying 100% strain, along with its schematic illustration (right). Scale bars in (e) are 50 μm. (f) Photographs of the counter-contacting layers and the bottom layers used to evaluate triboelectric properties. (g) Measured Q_{SC} and V_{OC} for Ecoflex-CNT with g-IPN synthesized using pAA ($t_{IPN,equiv}$ = 75 nm) and its control groups, using various counter-contacting materials.
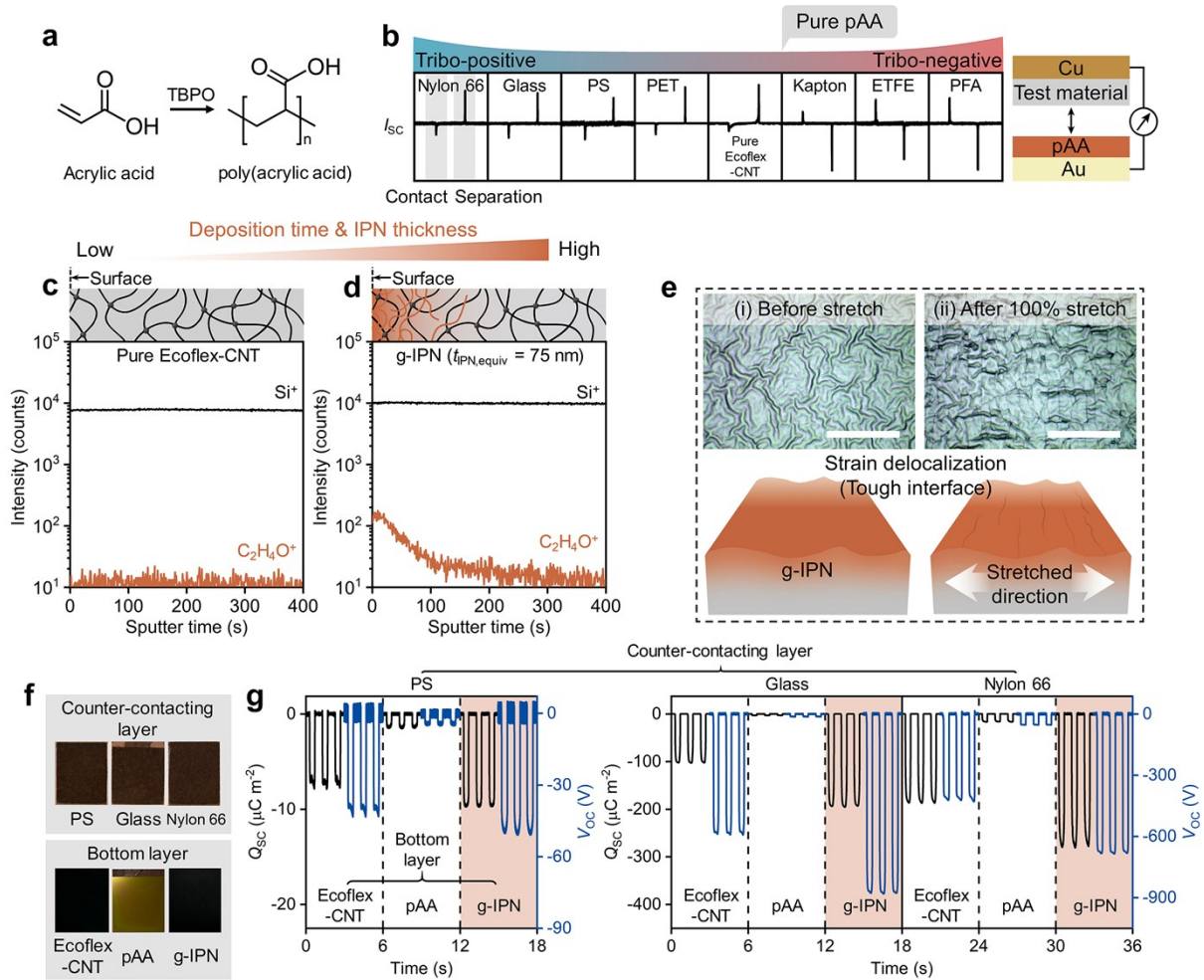
Figure S11. Output performance of 2D-IPN-TENG with ETFE as a counter-contacting material. (a) and (b) Measured Q_{SC} and V_{OC} for various $t_{IPN,equiv}$. (c) Measured charging ratio (η_Q) for extreme $t_{IPN,equiv}$ ($t_{IPN,equiv}$ = 0 nm and 1000 nm) and for the optimized $t_{IPN,equiv}$ ($t_{IPN,equiv}$ = 75 nm). (d) Extracted charge accumulation cycle (τ_{90}) for various $t_{IPN,equiv}$.
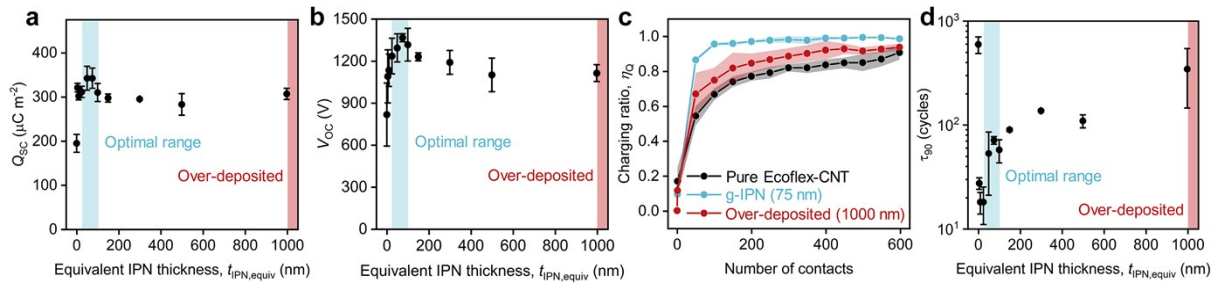
Figure S12. Output performance of 2D-IPN-TENG with PFA as a counter-contacting material. (a) and (b) Measured Q_{SC} and V_{OC} for various $t_{IPN,equiv}$. (c) Measured charging ratio (η_Q) for extreme $t_{IPN,equiv}$ ($t_{IPN,equiv}$ = 0 nm and 1000 nm) and for the optimized $t_{IPN,equiv}$ ($t_{IPN,equiv}$ = 75 nm). (d) Extracted charge accumulation cycle (τ_{90}) for various $t_{IPN,equiv}$.
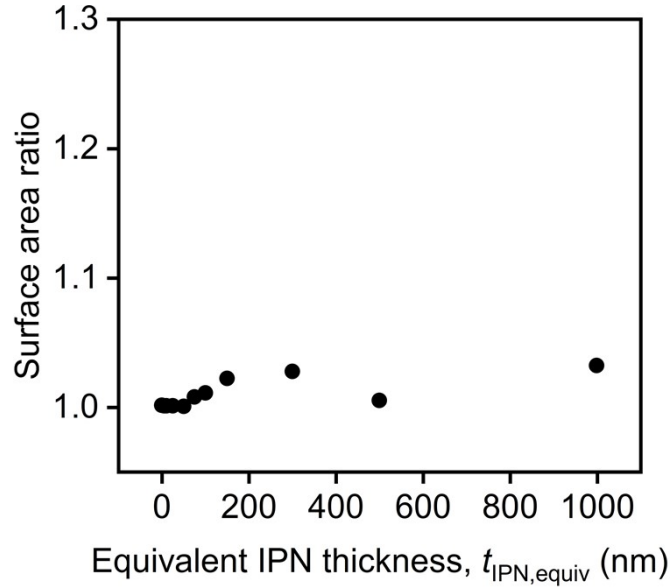
Figure S13. Surface area ratio of Ecoflex-CNT with g-IPN for various $t_{IPN,equiv}$. Here, the surface area ratio is defined as the ratio between the actual surface area measured by AFM and the nominal scanned area (100 μm × 100 μm). Across the entire range of $t_{IPN,equiv}$, the surface area ratios were not sufficient to significantly influence the output performance of the 2D-IPN-TENG, according to previous works that studied the relation between the surface area ratio and the magnitude of CE.[2,3]
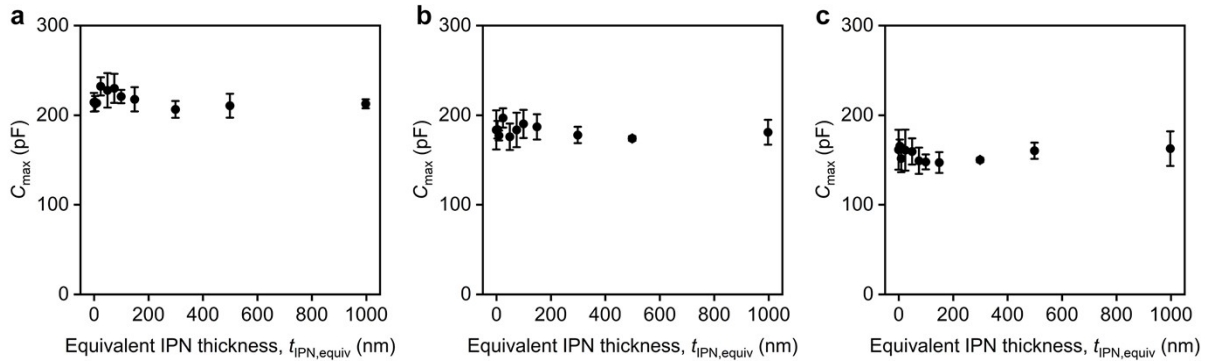
Figure S14. Measured C_{max} of 2D-IPN-TENG for various $t_{IPN,equiv}$. (a) C_{max} of 2D-IPN-TENG for various $t_{IPN,equiv}$, with Kapton as a counter-contacting material. (b) C_{max} of 2D-IPN-TENG for various $t_{IPN,equiv}$, with ETFE as a counter-contacting material. (c) C_{max} of 2D-IPN-TENG for various $t_{IPN,equiv}$, with PFA as a counter-contacting material. For all counter-contacting materials, the C_{max} of the 2D-IPN-TENG remained constant across the entire range of $t_{IPN,equiv}$.
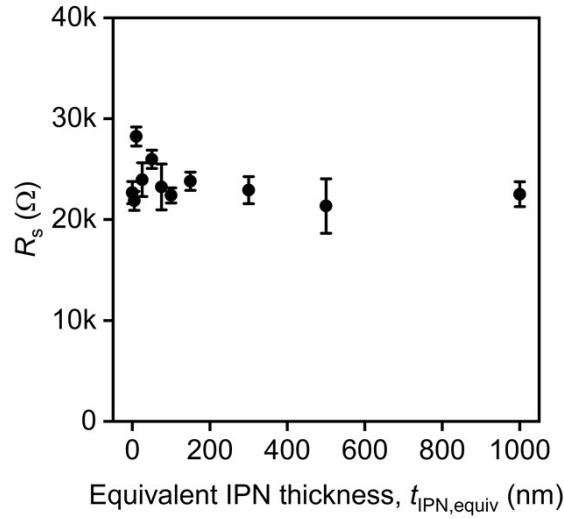
Figure S15. Measured R_s of Ecoflex-CNT with g-IPN for various $t_{IPN,equiv}$. The R_s of Ecoflex-CNT with g-IPN remained constant across the entire range of $t_{IPN,equiv}$.
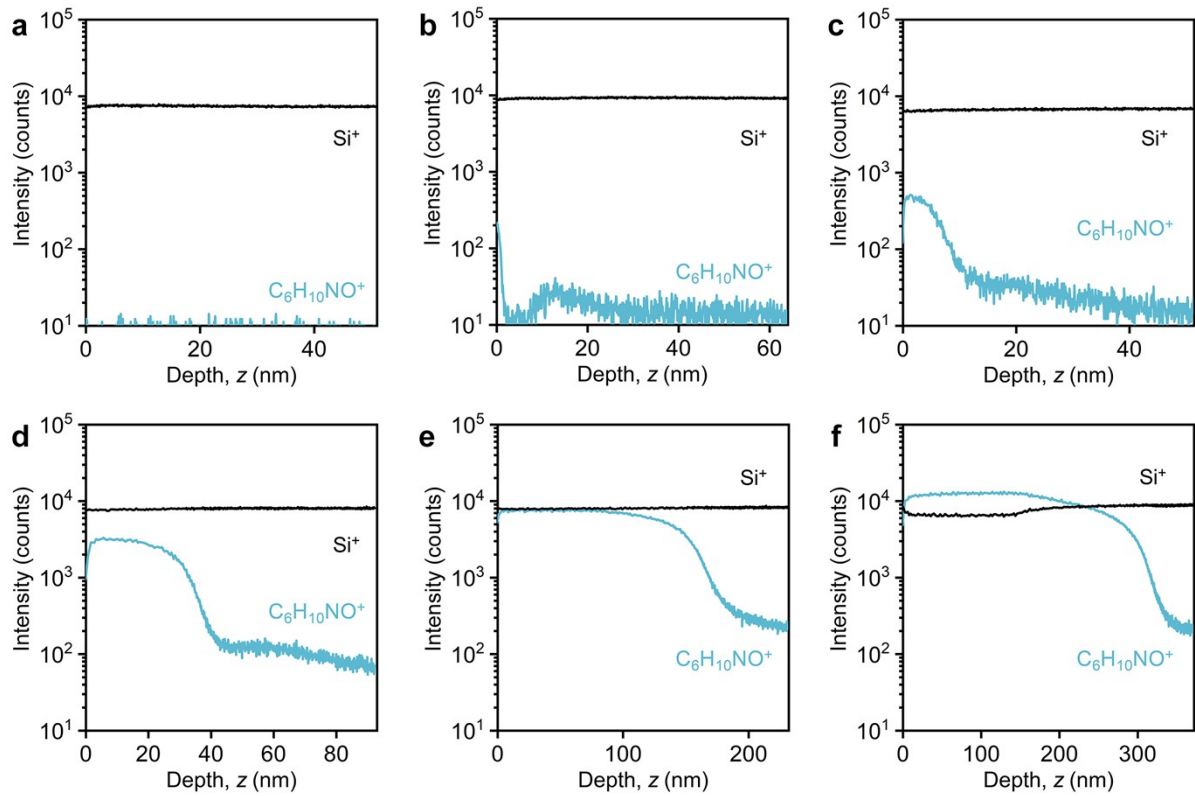
Figure S16. Calibrated ToF-SIMS depth profiles of Ecoflex-CNT with g-IPN for various $t_{IPN,equiv}$. Calibrated ToF-SIMS depth profiles of Ecoflex-CNT with g-IPN, obtained at $t_{IPN,equiv}$ of (a) 0 nm, (b) 10 nm, (c) 75 nm, (d) 150 nm, (e) 500 nm, and (f) 1000 nm, are shown.
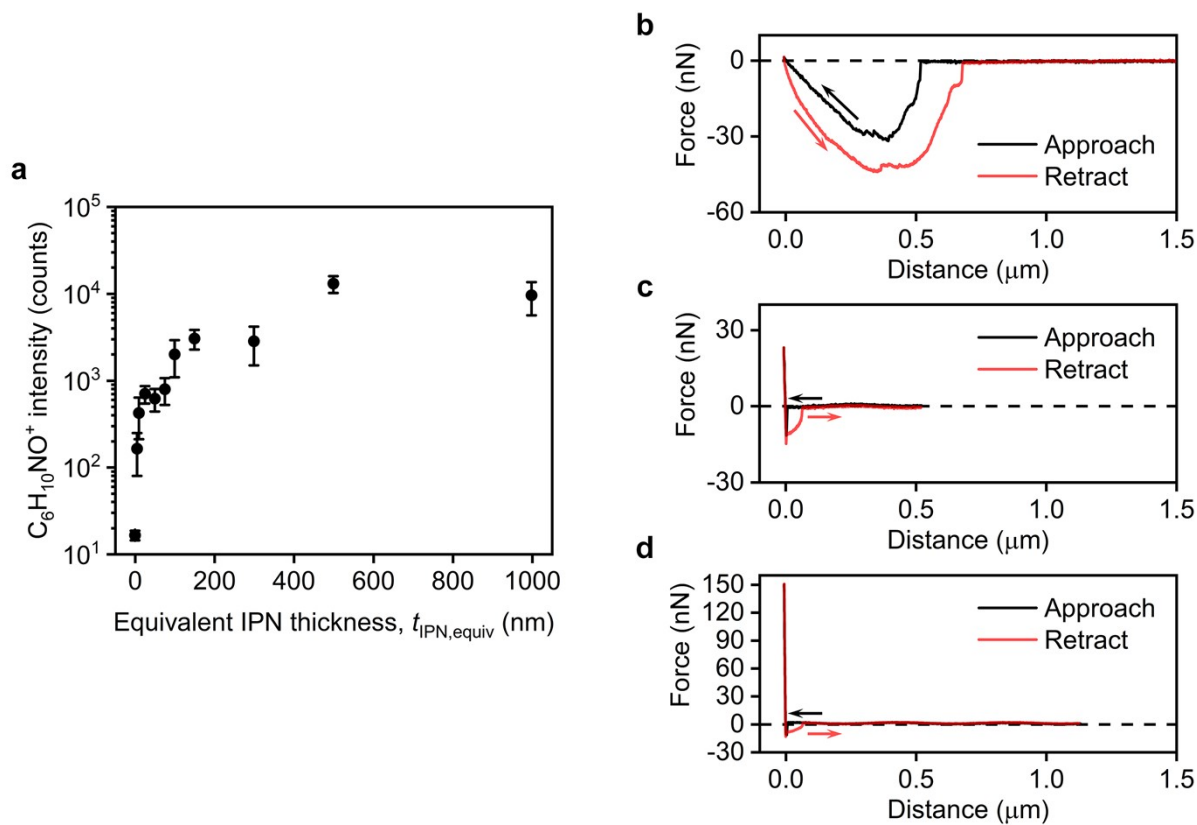
Figure S17. Surface ToF-SIMS intensity and *F-d* spectroscopy measurements used to calculate RCA. (a) Measured surface ToF-SIMS intensity of Ecoflex-CNT with g-IPN for various $t_{\text{IPN,equiv}}$. $C_6H_{10}NO^+$ represents a characteristic fragment ion of pVP. Examples of force-distance (*F-d*) curves measured on the surface of Ecoflex-CNT with g-IPN, at $t_{\text{IPN,equiv}}$ of (b) 0 nm, (c) 75 nm, and (d) 1000 nm, are shown.
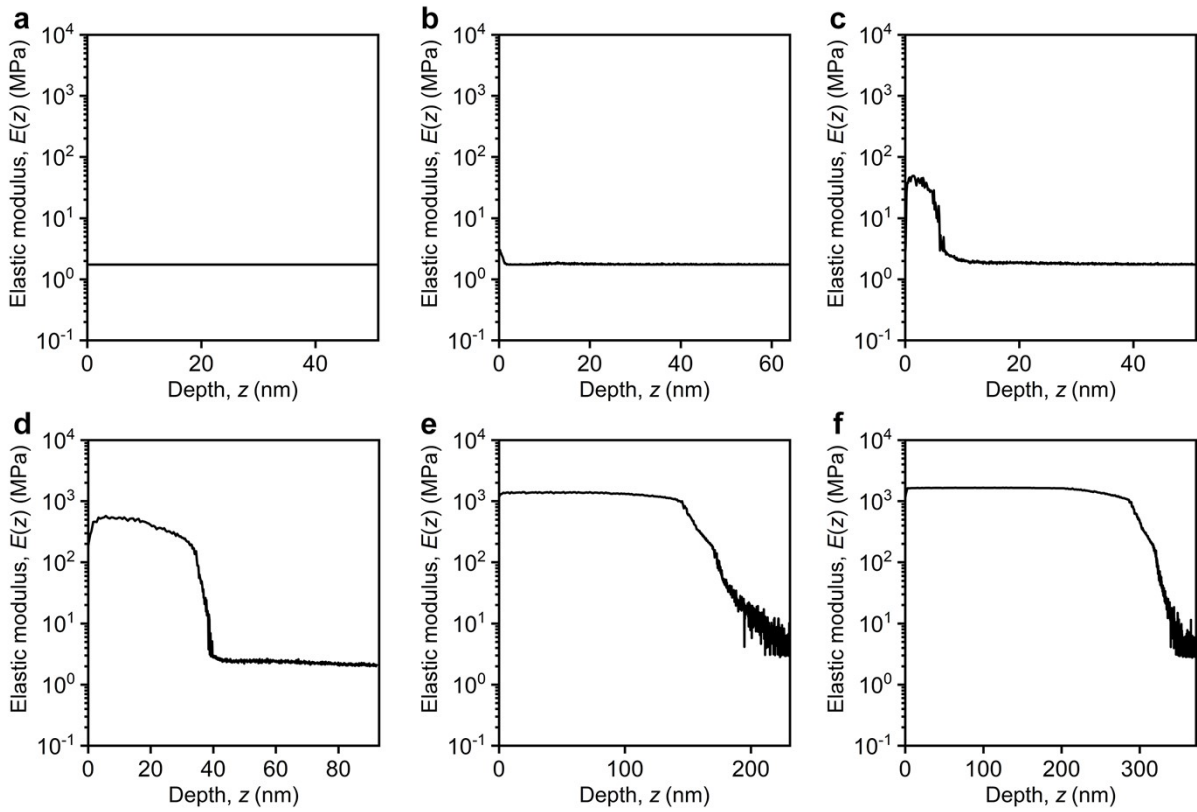
Figure S18. Depth profiles of elastic modulus ($E(z)$) of Ecoflex-CNT with g-IPN for various $t_{IPN,equiv}$. Depth profiles of elastic modulus ($E(z)$) of Ecoflex-CNT with g-IPN at $t_{IPN,equiv}$ of (a) 0 nm, (b) 10 nm, (c) 75 nm, (d) 150 nm, (e) 500 nm, and (f) 1000 nm, are shown.
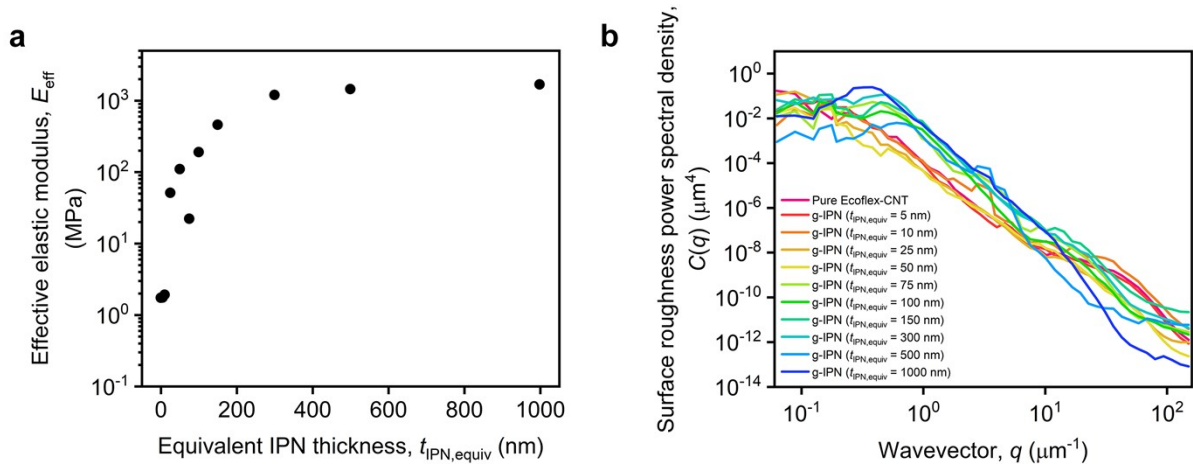
Figure S19. E_{eff} and $C(q)$ used to calculate RCA. (a) Calculated E_{eff} of Ecoflex-CNT with g-IPN at various $t_{IPN,equiv}$. (b) Experimentally measured $C(q)$ of Ecoflex-CNT with g-IPN at various $t_{IPN,equiv}$.
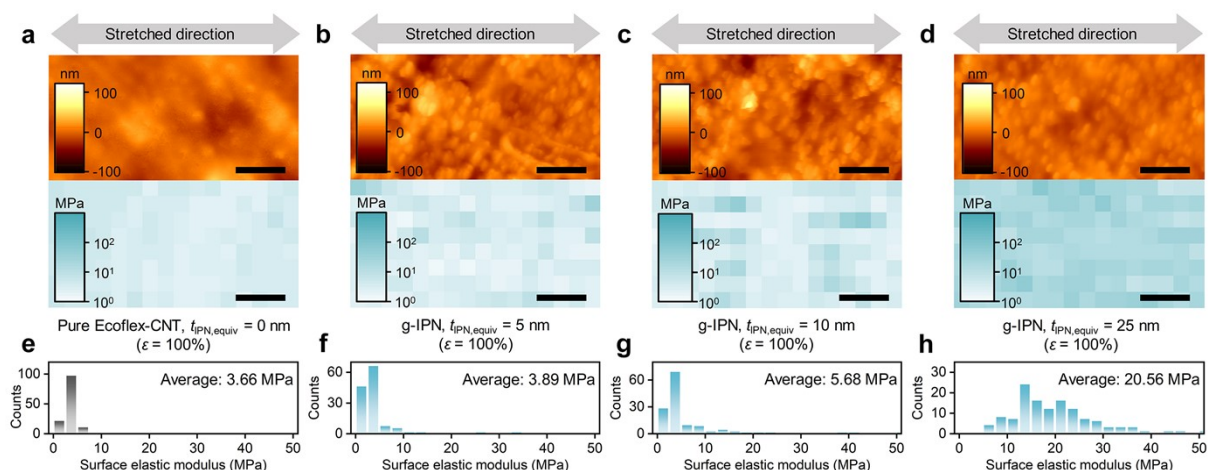
Figure S20. Surface elastic modulus mappings of Ecoflex-CNT with g-IPN under stretched (ε = 100%) state for $t_{IPN,equiv}$ of 25 nm or less. The AFM topography images (top) and their corresponding surface elastic modulus mappings (bottom) obtained from stretched (ε = 100%) Ecoflex-CNT with g-IPN at $t_{IPN,equiv}$ of (a) 0 nm, (b) 5 nm, (c) 10 nm, and (d) 25 nm, are shown. Scale bars in (a)-(d) are 500 nm. The distribution of the surface elastic modulus, obtained from the stretched (ε = 100%) Ecoflex-CNT with g-IPN at $t_{IPN,equiv}$ of (e) 0 nm, (f) 5 nm, (g) 10 nm, and (h) 25 nm, are shown. For $t_{IPN,equiv}$ of 25 nm or less, the surface elastic modulus mappings and the distribution of surface elastic modulus reveal that the surface elastic modulus is spatially uniform and has no distinct orientation, unlike the observations at $t_{IPN,equiv}$ = 75 nm (Figure 5d and f). This indicates that the Ecoflex-CNT with g-IPN, at $t_{IPN,equiv}$ of 25 nm or less, is intrinsically stretchable. Furthermore, the similar average surface elastic modulus between Figure S20h and Figure 5f suggests that the intrinsically stretchable IPN with $t_{IPN,equiv}$ around 25 nm is exposed to the ambient when the Ecoflex-CNT with g-IPN of $t_{IPN,equiv}$ = 75 nm is stretched.
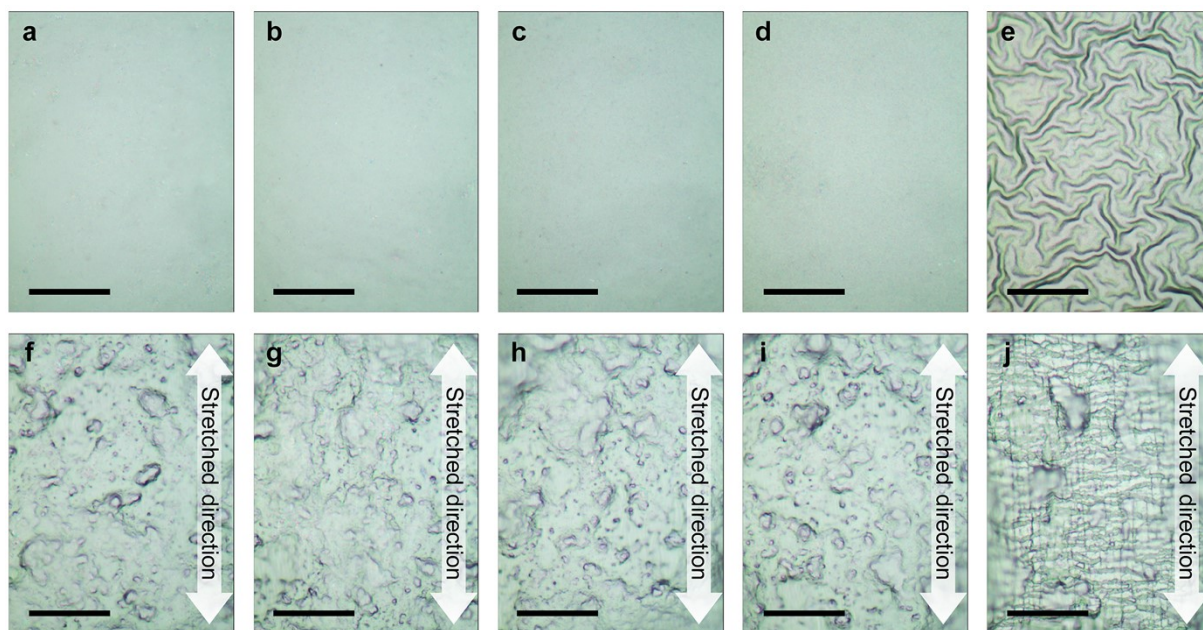
Figure S21. OM images of Ecoflex-CNT with g-IPN under unstretched ($\varepsilon = 0\%$) and stretched ($\varepsilon = 100\%$) states for various $t_{\text{IPN,equiv}}$. OM images of unstretched ($\varepsilon = 0\%$) Ecoflex-CNT with g-IPN at $t_{\text{IPN,equiv}}$ of (a) 0 nm, (b) 5 nm, (c) 10 nm, (d) 25 nm, and (e) 75 nm, are shown. OM images of stretched ($\varepsilon = 100\%$) Ecoflex-CNT with g-IPN at $t_{\text{IPN,equiv}}$ of (f) 0 nm, (g) 5 nm, (h) 10 nm, (i) 25 nm, and (j) 75 nm, are shown. Scale bars in (a)-(j) are 50 μm. For (a)-(d), no distinct wrinkles are observed, unlike in (e). This indicates that the difference in elastic modulus between the surface and the substrate (pure Ecoflex-CNT) is relatively low when $t_{\text{IPN,equiv}}$ is 25 nm or less, compared to when $t_{\text{IPN,equiv}} = 75$ nm. Moreover, when Ecoflex-CNT with g-IPN at $t_{\text{IPN,equiv}}$ of 25 nm or less is stretched, no distinct directional wrinkles or cracks are observed in the OM images, while they are clearly observed for $t_{\text{IPN,equiv}} = 75$ nm. This supports that Ecoflex-CNT with g-IPN at $t_{\text{IPN,equiv}}$ of 25 nm or less is intrinsically stretchable.
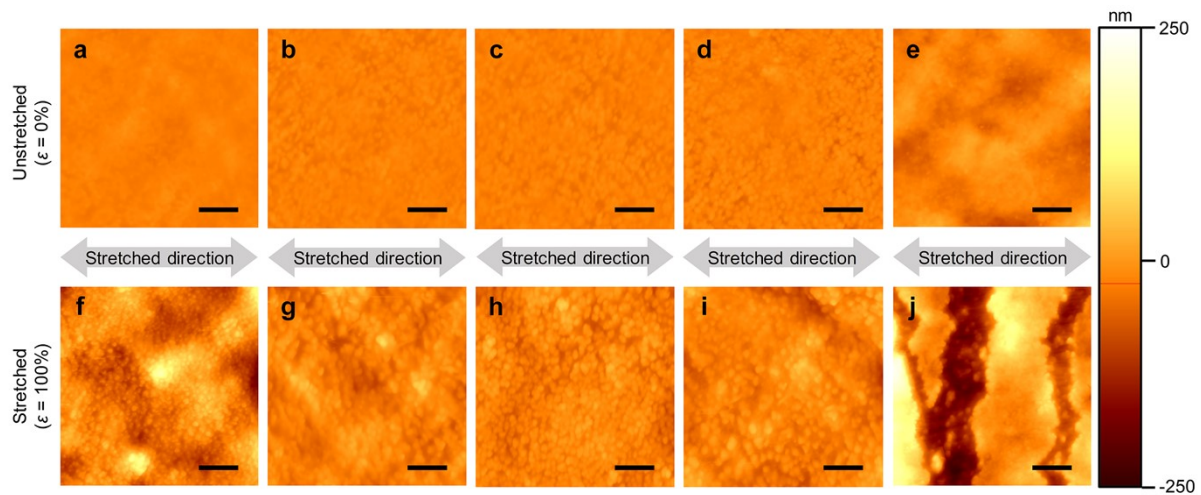
Figure S22. AFM topography images of Ecoflex-CNT with g-IPN under unstretched (ε = 0%) and stretched (ε = 100%) states for various $t_{\text{IPN,equiv}}$. AFM topography images of unstretched (ε = 0%) Ecoflex-CNT with g-IPN at $t_{\text{IPN,equiv}}$ of (a) 0 nm, (b) 5 nm, (c) 10 nm, (d) 25 nm, and (e) 75 nm, are shown. AFM topography images of stretched (ε = 100%) Ecoflex-CNT with g-IPN at $t_{\text{IPN,equiv}}$ of (f) 0 nm, (g) 5 nm, (h) 10 nm, (i) 25 nm, and (j) 75 nm, are shown. Scale bars in (a)-(j) are 1 μm. Similar to the OM images shown in Figure S21, for $t_{\text{IPN,equiv}}$ of 25 nm or less, no distinct orientations on the surface are observed when they are stretched, as shown in (f)-(i). In contrast, for $t_{\text{IPN,equiv}}$ = 75 nm, microcracks are clearly observed along the direction of stretch, as shown in (j). This supports that Ecoflex-CNT with g-IPN at $t_{\text{IPN,equiv}}$ of 25 nm or less is intrinsically stretchable.
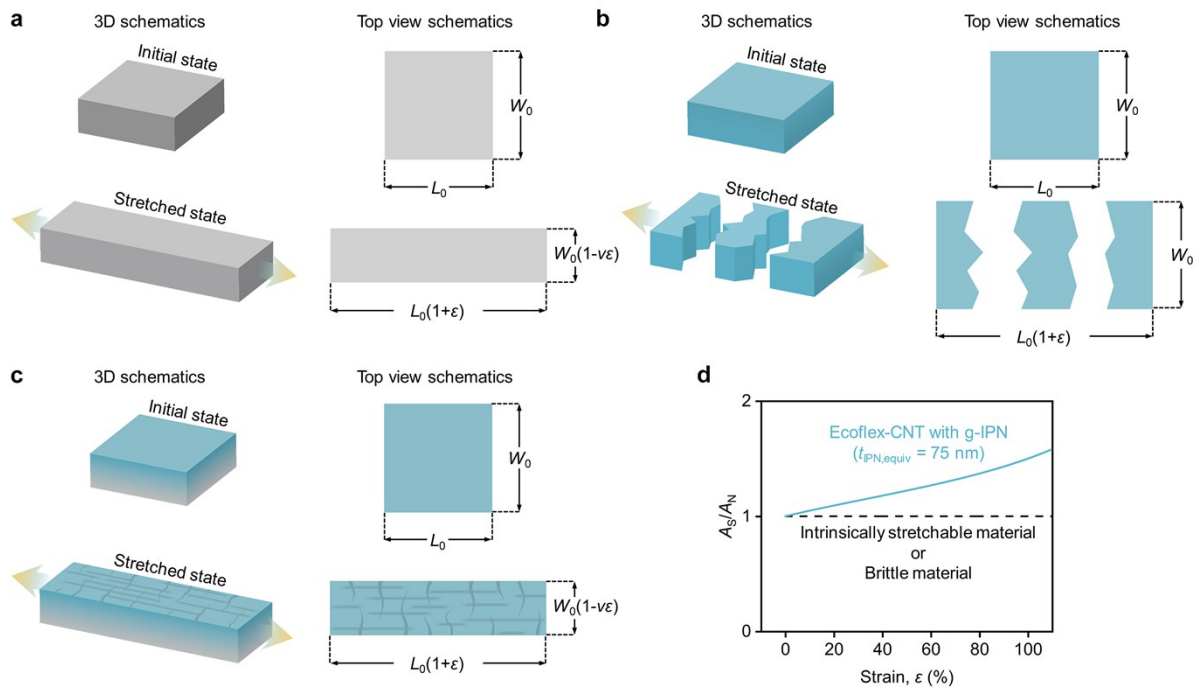
Figure S23. Simple analytical model describing the increase in surface area of the Ecoflex-CNT with g-IPN ($t_{\text{IPN,equiv}}$ = 75 nm) under increasing strain. 3D schematics and top view schematics depicting the initial and stretched states of (a) an intrinsically stretchable material, (b) a brittle material, and (c) Ecoflex-CNT with g-IPN ($t_{\text{IPN,equiv}}$ = 75 nm). In the stretched state of (c), cracks along the direction of stretch and wrinkles along the direction perpendicular to stretch are shown. For (a)-(c), L_0, W_0, ε, and v denote the initial length of a sample, the initial width of a sample, the strain applied to a sample, and the Poisson's ratio of the intrinsically stretchable material, respectively. (d) Calculated ratio of the surface area (A_S) to the nominal area (A_N).
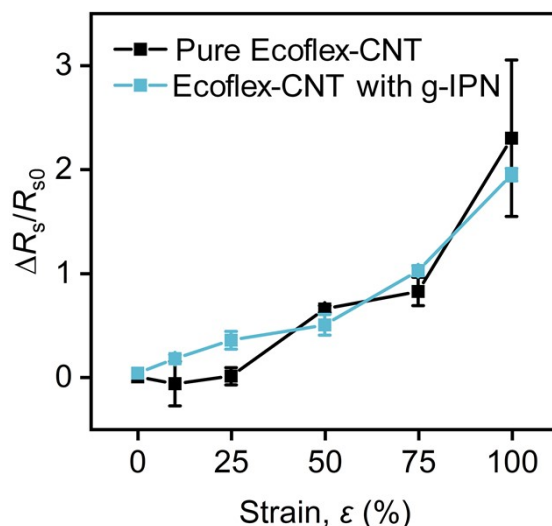
Figure S24. Measured R_s of pure Ecoflex-CNT and Ecoflex-CNT with g-IPN ($t_{IPN,equiv}$ = 75 nm) under various strains. The change in R_s relative to the unstrained state ($\Delta R_s/R_{s0}$) was similar in both Ecoflex-CNT with and without g-IPN, where $\Delta R_s = R_s$ (with strain) - R_{s0} (without strain).
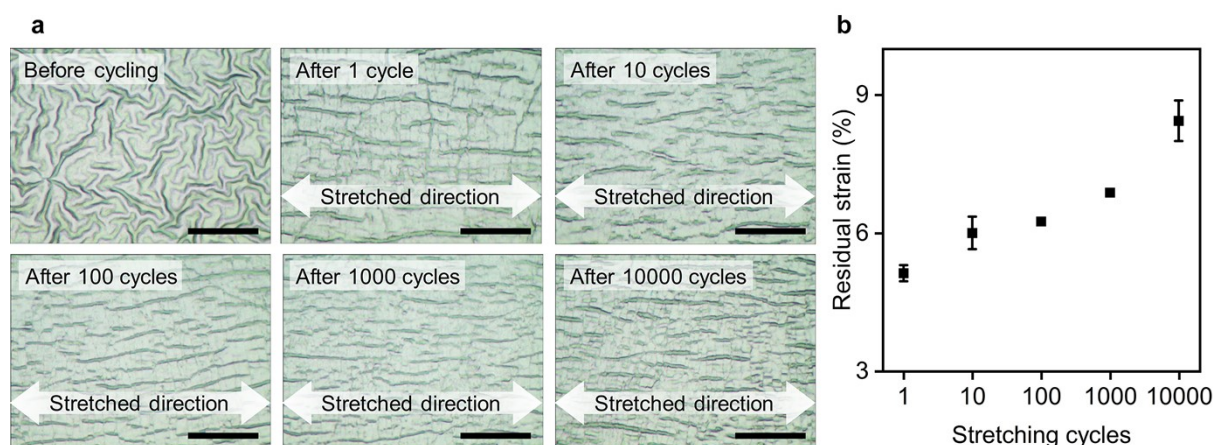
Figure S25. OM images and residual strain of Ecoflex-CNT with g-IPN ($t_{IPN,equiv}$ = 75 nm), released after various iterative stretching (ε = 100%) and releasing cycles. (a) OM images of Ecoflex-CNT with g-IPN ($t_{IPN,equiv}$ = 75 nm), released after various stretching cycles. Scale bars are 50 μm. (b) Measured residual strain of Ecoflex-CNT with g-IPN ($t_{IPN,equiv}$ = 75 nm) released after various stretching cycles. In (a), even after 10,000 stretching cycles, the intrinsically stretchable IPN layer was not exposed; only the traces of microcracks were observed. Moreover, the residual strain caused the randomly oriented wrinkles to smooth out, resulting in a reduced surface area of Ecoflex-CNT with g-IPN.
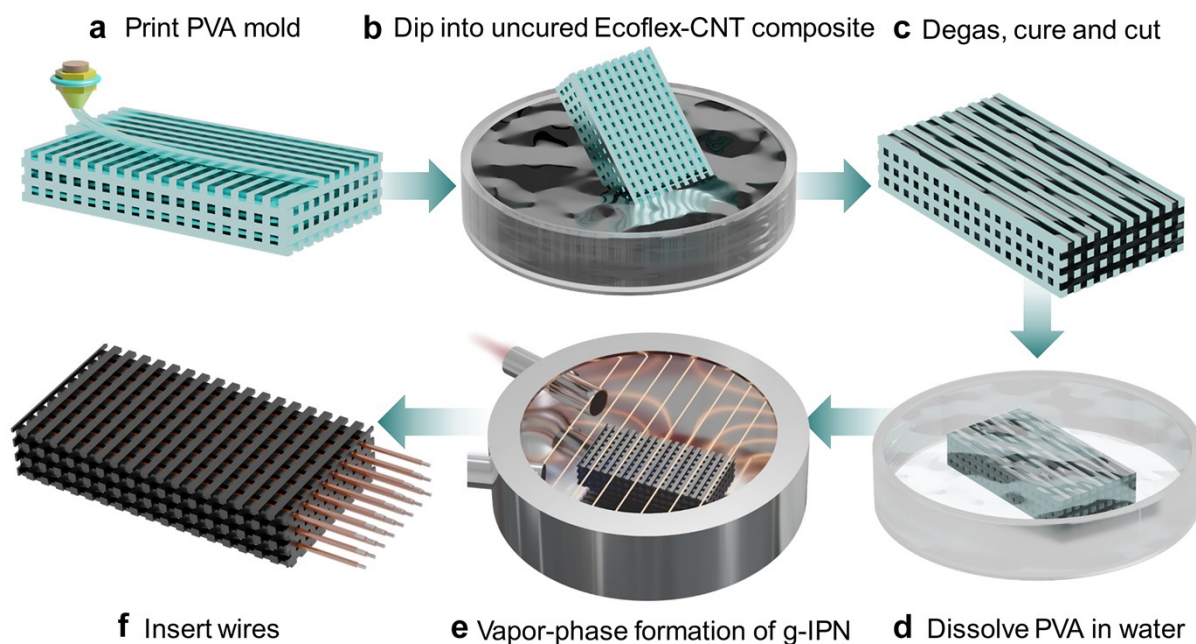
Figure S26. Fabrication process of the 3D-TENG and 3D-IPN-TENG. As described in the Experimental section, 3D-TENG and 3D-IPN-TENG were fabricated by: (a) printing a sacrificial PVA mold with the inverse structure of the desired Ecoflex-CNT sponge, (b) dipping the PVA mold into uncured Ecoflex-CNT, (c) degassing and curing the Ecoflex-CNT and cutting off the residuals, (d) selectively dissolving the PVA mold in hot water, (e) forming g-IPN by the iCVD process, but only for 3D-IPN-TENG, and (f) inserting wires into the lengthy pores of the Ecoflex-CNT sponge.
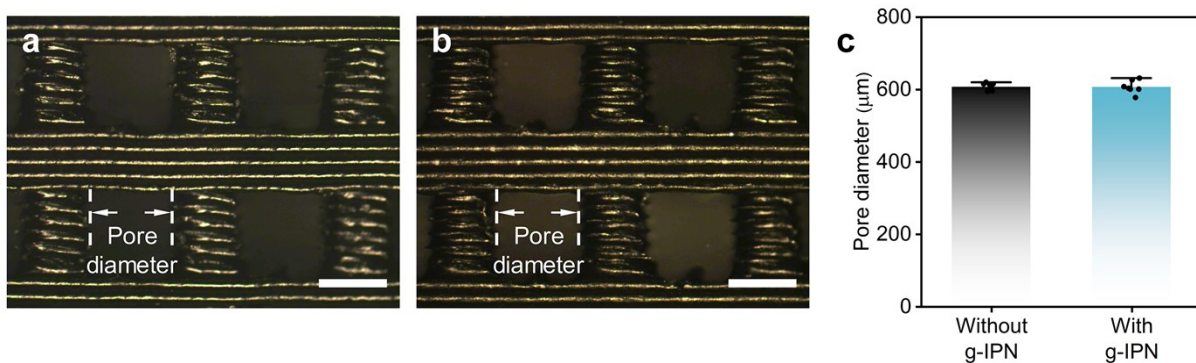
Figure S27. Measured pore diameter of Ecoflex-CNT sponges with and without g-IPN. OM images showing the pore diameter of the Ecoflex-CNT sponges, (a) without g-IPN and (b) with g-IPN. Scale bars in (a) and (b) are 500 μm. (c) Pore diameter distribution of the Ecoflex-CNT sponges, both with and without g-IPN.
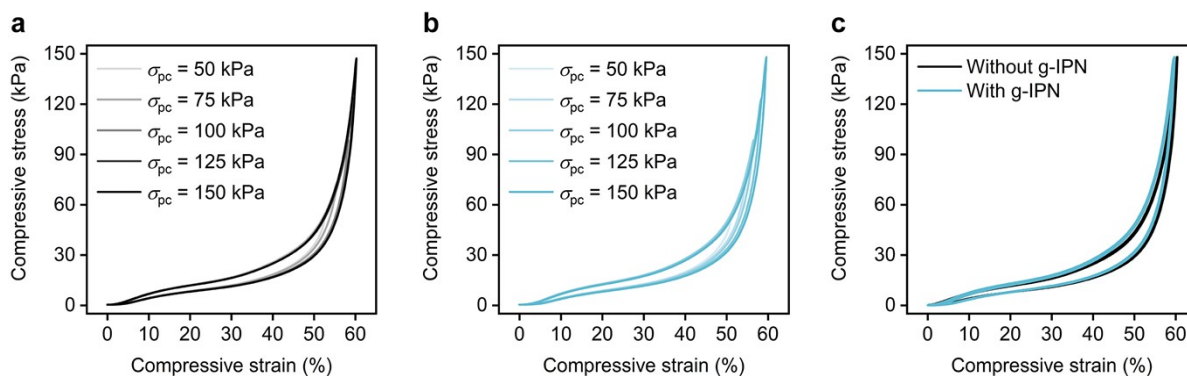
Figure S28. Compressive stress-strain curves for Ecoflex-CNT sponges with and without g-IPN. (a) Measured compressive stress-strain curves of an Ecoflex-CNT sponge without g-IPN under various peak compressive stresses. (b) Measured compressive stress-strain curves of an Ecoflex-CNT sponge with g-IPN under various peak compressive stresses. For (a) and (b), the peak compressive stress is denoted as σ_{pc}. (c) Comparison of the measured compressive stress-strain curves for Ecoflex-CNT sponges with and without g-IPN, during 10 cycles of periodic compression and relaxation. For (c), σ_{pc} was set at 150 kPa. For (a)-(c), no noticeable differences in mechanical properties between the Ecoflex-CNT sponges with and without g-IPN were observed.
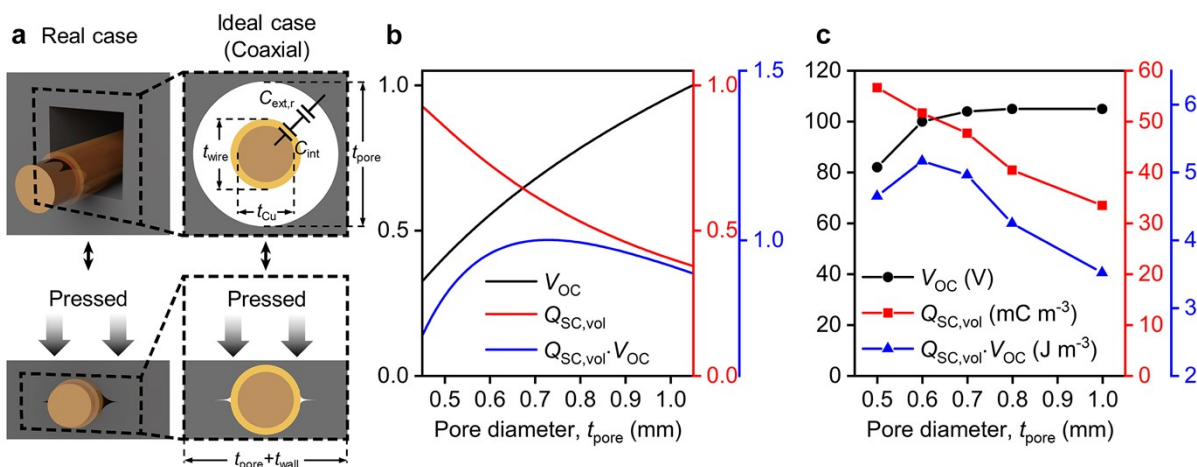
Figure S29. Theoretical and experimental optimization of pore diameter for the sponge-structured 3D elastic TENGs. (a) 3D schematics of the real case (left column) and 2D cross-sectional schematics of the ideal case (right column). In the ideal case, a pore and a wire are aligned coaxially. In the ideal case, $C_{ext,r}$, C_{int}, t_{pore}, t_{wire}, t_{Cu}, and t_{wall} denote the capacitance between the outer surface of a wire and the Ecoflex-CNT sponge in the relaxed state, the capacitance between the outer surface of a wire and the copper core in a wire, the pore diameter, the outer diameter of a wire, the diameter of the copper core in a wire, and the thickness of the Ecoflex-CNT wall between adjacent pores, respectively. (b) Theoretical V_{OC}, $Q_{SC,vol}$, and their product for various pore diameters. All three parameters are normalized by their peak values for convenience. (c) Experimentally measured V_{OC}, $Q_{SC,vol}$, and their product for various pore diameters.
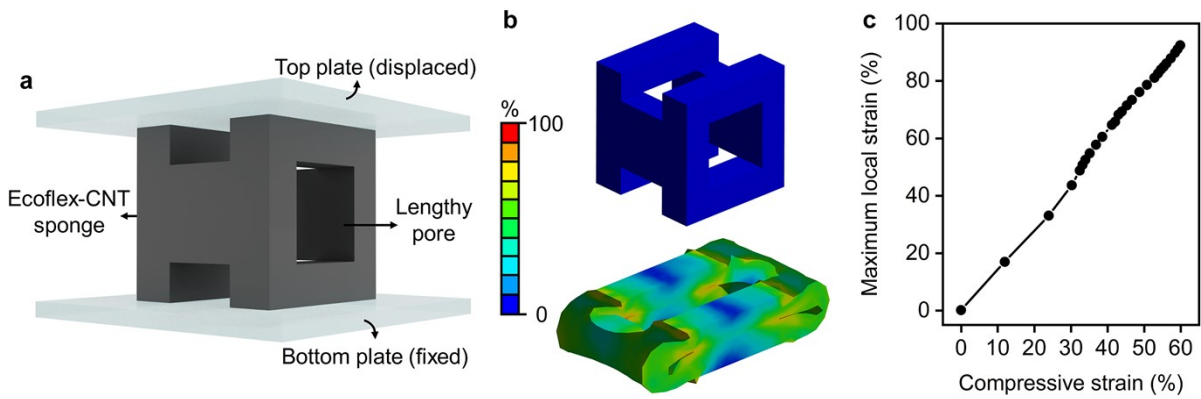
Figure S30. FEM simulation of the compression of Ecoflex-CNT sponge with g-IPN. (a) 3D schematic of the geometry used in the FEM simulation. The unit cell structure of the 3D-structured sponge was used for the FEM simulation. (b) The distribution of local strain throughout the unit cell structure of the Ecoflex-CNT sponge with g-IPN, before compression (top) and after compression with a compressive strain of 60% (bottom). (c) Maximum local strain along the lengthy pore in the unit cell structure under various compressive strains.
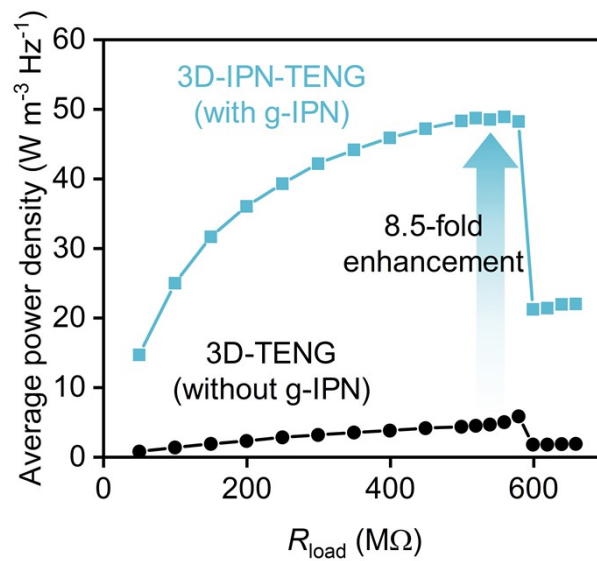
Figure S31. Comparison of average power density between the 3D-TENG and 3D-IPN-TENG. The maximum average power density of the 3D-IPN-TENG was approximately 8.5-fold higher than that of the 3D-TENG.
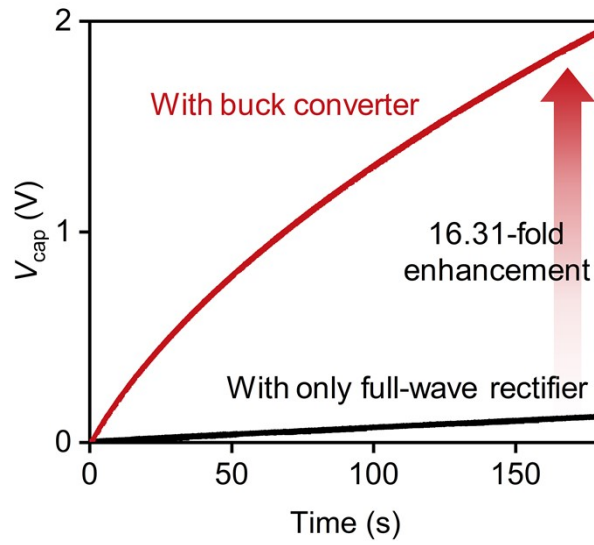
Figure S32. Comparison of V_{cap} between a PMC composed of a full-wave rectifier and a buck converter and one with only a full-wave rectifier. In both cases, the capacitance of the output capacitor was 3.3 mF. When a PMC consisting of a full-wave rectifier and a buck converter was used, the V_{cap} after 180 seconds of charging with the 3D-IPN-TENG was approximately 16.31-fold higher than when only a full-wave rectifier was used as a PMC.

Reference	Materials	Output enhancement strategy	Output performance			Mechanical properties	
			Q_{SC} (µC m^{-2})	V_{OC} (V)	Peak power density (W m^{-2})	Bulk elastic modulus (kPa)	Elongation at break (%)
4	TPU/Carbon black & PTFE	Charge injection	17.5	41	0.00495	27150*	646
5	Ecoflex/porous carbon & PDMS	Trap construction	135	115.9	0.13	60	570
6	Silicone rubber & Al	Pre-straining	-	44.16	1.03	397*	567
7	Ecoflex/SiO$_2$ electret & Nitrile rubber	Charge injection	205.6	1090	2.28	36.27*	796
8	Crumpled graphene & PDMS	Pre-straining	178.98	83	2.5	-	-
9	Porous PDMS-Ecoflex/ MXene foam & Nylon fabric	Filler incorporation	150	73.6	2.76	-	-
10	Conductive ink & PTFE	Pre-straining	162.6*	128	2.86	-	-
11	Porous TPU/BTO/MXene & Microdome PDMS	Filler incorporation	2170	260	6.65	-	-
12	Silicone rubber/Nylon powder & Silicone rubber	Filler incorporation	125	1170	11.2	6479*	120
13	Silicone rubber/MoO$_3$/MOF-525 & Human skin	Filler incorporation	228.8	1760	18.38	-	250
14	Silicone rubber/V$_2$CT$_x$ & Nylon fabric	Filler incorporation	750	380	19.75	-	420 (with serpentine structure)
15	PVDF/PDMS & Al	Trap construction	835	216	20.8	-	-
This work	**Ecoflex-CNT with g-IPN & Kapton**	**Complementary material synthesis**	**445**	**1335**	**22.06**	**207.5**	**530**

Table S1. Systematic comparison of output performance and mechanical properties with previous works on stretchable TENGs.

*These values were inferred from the data in the references.

Table S2. Systematic comparison of output performance between 2D-IPN-TENG and 3D-IPN-TENG.

	$Q_{SC,vol}$ (mC m^{-3})	V_{OC} (V)	Maximum average power density (W m^{-3} Hz^{-1})
2D-IPN-TENG	24.42*	1450	2.7*
3D-IPN-TENG	267.2	455	**48.9**

* These volume-normalized values were calculated based on the maximum separation distance of the 2D-IPN-TENG (1.8 cm).

As shown in Table S2, the volume-normalized maximum average power density, which is directly related to the amount of energy generated during a single contact-separation cycle (or compression-relaxation for the 3D-IPN-TENG) from a certain volume, was significantly higher in the 3D-IPN-TENG than in the 2D-IPN-TENG. This indicates that the volumetric efficiency of the 3D-IPN-TENG is substantially higher than that of the 2D-IPN-TENG due to its 3D sponge structure.

Note S1. Tape peeling experiment and subsequent ToF-SIMS analyses.

The difference in interfacial toughness between Ecoflex-CNT with drop-cast pVP (Case I) and Ecoflex-CNT with g-IPN (Case II, $t_{IPN,equiv} = 75$ nm) was analyzed using a simple tape peeling experiment (Figure S6a).[16] For a fair comparison between both cases, pVP synthesized by iCVD was used in Case I. First, commercial Kapton tape was gently pressed onto the surfaces of both samples. After pressing for 10 seconds, the tape was peeled off from both samples. As shown in Figure S6b and c, the boundaries between the intact areas and the tape-peeled areas in both samples were clearly visible in the OM images. Notably, the rainbow-like colors in Case I disappeared in the tape-peeled area (Figure S6b), indicating the complete delamination of the drop-cast pVP layer. To precisely characterize the surfaces of both samples, they were immediately loaded into the ToF-SIMS equipment after tape peeling, to obtain their ToF-SIMS depth profiles. The experimental details of the ToF-SIMS analyses are described in the Experimental section.

The ToF-SIMS depth profiles were obtained from both intact and tape-peeled areas in Case I and Case II. In Case I, abrupt depth profiles of $C_6H_{10}NO^+$ intensity (the characteristic fragment ion of pVP) and Si^+ intensity (the characteristic fragment ion of Ecoflex-CNT) were obtained from the intact area (Figure S6d). The results suggest that a pure pVP layer existed on the surface of Ecoflex-CNT, at the intact area of Case I. In contrast, in the tape-peeled area of Case I, $C_6H_{10}NO^+$ was not detected, whereas constant Si^+ intensity was obtained throughout the entire depth profile (Figure S6e). This indicates that the pure pVP layer was completely delaminated from the Ecoflex-CNT by tape peeling. In Case II, similar to the result shown in Figure 2f, a gradient depth profile of $C_6H_{10}NO^+$ intensity and a constant depth profile of Si^+ intensity were obtained from the intact area (Figure S6f). Similarly, in the tape-peeled area of Case II, the gradient depth profile of $C_6H_{10}NO^+$ intensity and the intensity value of $C_6H_{10}NO^+$ near the surface remained almost identical to those in the intact area (Figure S6g). This implies that the g-IPN was not delaminated even after tape peeling.

The results from the tape peeling experiment and subsequent ToF-SIMS analyses prove that Case II (Ecoflex-CNT with g-IPN) had a significantly higher interfacial toughness compared to Case I (Ecoflex-CNT with drop-cast pVP). Moreover, the absence of $C_6H_{10}NO^+$ in the tape-peeled area of Case I indicates that an IPN between pVP and Ecoflex-CNT cannot be formed by drop-casting. Therefore, the superior mechanical and triboelectric properties of Case II, compared to those of Case I, are attributed to the presence of the IPN layer.

Note S2. Bulk mechanical and triboelectric properties of the uniform IPN (Case III).

To investigate the influence of the depth-directional gradient profile of the IPN on bulk mechanical and triboelectric properties, Ecoflex-CNT with g-IPN (Case II, $t_{\text{IPN,equiv}}$ = 75 nm) and Ecoflex-CNT with uniformly formed IPN throughout the entire sample (Case III) were prepared. As in Case II, the guest polymer (*i.e.*, pVP) was polymerized to form IPN after the polymerization of the host polymer (*i.e.*, Ecoflex-CNT) to prepare Case III. However, to synthesize the uniform IPN without a depth-directional concentration gradient of pVP, samples for Case III were prepared using a conventional solution-based process instead of iCVD.[17,18]

As shown in Figure S8a, pure Ecoflex-CNT samples were immersed in a mixture of *N*-vinyl-2-pyrrolidone (NVP) monomer, *tert*-butyl peroxide (TBPO) initiator, and a solvent. For the preparation of Case III, tetrahydrofuran (THF) was selected as the solvent because it could dissolve both NVP and TBPO and could significantly swell the Ecoflex-CNT samples,[19] allowing NVP and TBPO molecules to diffuse easily into the Ecoflex-CNT samples. Although the swelling of the Ecoflex-CNT samples ended within 30 minutes after immersion in the mixture, the samples were immersed in the mixture for 4 hours to ensure the uniform distribution of NVP and TBPO molecules within the Ecoflex-CNT samples. Afterwards, the swollen samples were removed from the mixture and were immediately placed on a pre-heated hot plate at 140 °C to vaporize the THF remaining inside the samples and to initiate the polymerization of NVP by thermally decomposing TBPO into *tert*-butoxy radicals. After heating the samples for 30 minutes, they were naturally cooled and were used for subsequent experiments.

The concentration of pVP in Case III can be controlled by the concentration of NVP in the mixture. For a fair comparison between Case II and Case III, the concentration of NVP in the mixture was adjusted so that the surface elastic modulus in Case III became comparable to that in Case II. Consequently, a volumetric ratio of THF : NVP : TBPO = 50 : 4 : 1 was used to prepare the mixture, which resulted in an average surface elastic modulus of 261.54 MPa. Note that this surface elastic modulus value of the sample in Case III was between that of g-IPN with $t_{\text{IPN,equiv}}$ = 75 nm and that of g-IPN with $t_{\text{IPN,equiv}}$ = 100 nm (Figure 4f). A photograph of the as-prepared samples of the pure Ecoflex-CNT, Case II, and Case III is shown in Figure S8b. In contrast to Case II, the sample in Case III was slightly contracted and distorted compared to the pure Ecoflex-CNT sample, possibly due to its increased swelling ratio in THF resulting from the formation of the IPN.[20]

The bulk mechanical properties of the pure Ecoflex-CNT, Case II, and Case III were comparatively analyzed (Figure S8c-f). While the bulk elastic modulus in Case II was similar to that of the pure Ecoflex-CNT due to the sub-micron thickness of the g-IPN, it increased significantly in Case III (Figure S8c and d). To further evaluate the stretchability of the samples, stress-strain curves were obtained during 10 iterative stretching ($\varepsilon = 100\%$) and releasing cycles for each case (Figure S8e). Although there were negligible differences between the pure Ecoflex-CNT and Case II, Case III exhibited an exceptionally high residual strain of around 60% (Figure S8e and f). This indicates that the degree of plasticity was substantially higher in Case III compared to that of the pure Ecoflex-CNT and Case II.

The triboelectric properties of the three cases were also comparatively analyzed. Q_{SC} was measured in the three cases while using Kapton as a counter-contacting material. As shown in Figure S8g, the Q_{SC} in Case III was even lower than that of the pure Ecoflex-CNT. The major reason for the low Q_{SC} in Case III was its low contact conformity, due to the high effective elastic modulus (E_{eff})[21] in Case III. Although the surface elastic modulus values in Case II and Case III were similar, the gradient structure in Case II effectively reduced its E_{eff}.[21] Therefore, the contact conformity between Kapton and Case III was lower than that between Kapton and Case II,[21] leading to a significantly lower Q_{SC} in Case III compared to that in Case II.[22,23] The influence of E_{eff} on contact conformity is further discussed in Figure 4 and Note S4.

Note S3. The demonstration of synergistic performance enhancement in Ecoflex-CNT with g-IPN synthesized using guest polymers other than pVP.

To demonstrate the universality of the complementary material synthesis strategy, it was shown that the synergistic performance enhancement could also be achieved by forming g-IPN on Ecoflex-CNT using guest polymers other than pVP. As alternative guest polymers, two polymers that can be synthesized by the iCVD process were selected: poly(1-vinylimidazole) (pVI) (Figure S9a) and poly(acrylic acid) (pAA) (Figure S10a). Both polymers were synthesized by free-radical polymerization using TBPO as the initiator.

Before the synthesis of g-IPN using pVI or pAA, the relative positions of pVI and pAA in the triboelectric series were investigated to characterize their electron-donating or electron-accepting tendencies. As shown in Figure S9b and S10b, seven materials ranging from the positive side to the negative side of the triboelectric series were selected as counter-contacting materials. Specifically, for pAA, pure Ecoflex-CNT was also selected as a counter-contacting material to determine the position of pAA in the triboelectric series relative to pure Ecoflex-CNT. To identify the relative positions of the two guest polymers in the triboelectric series, all counter-contacting materials were brought into contact with and separated from a pure pVI or a pure pAA film (each with a thickness of 3 μm) deposited on an Au substrate. For the case of pVI, the resulting waveforms of I_{SC} show that pVI was consistently positively charged, irrespective of the counter-contacting material. Therefore, pVI was placed at the positive end of the triboelectric series (Figure S9b). In contrast, for the case of pAA, the resulting waveforms of I_{SC} indicate that pAA was placed between pure Ecoflex-CNT and Kapton in the triboelectric series (Figure S10b). Therefore, pVI and pAA were more tribo-positive and tribo-negative than pure Ecoflex-CNT, respectively.

Subsequently, g-IPN was synthesized using pVI or pAA by depositing them on the pure Ecoflex-CNT samples with the iCVD process. The depth-directional gradient profiles of the g-IPN synthesized using pVI or pAA were confirmed using ToF-SIMS. In both cases, the characteristic fragment ion of pVI (*i.e.*, $C_5H_7N_2^+$)[24] or that of pAA (*i.e.*, $C_2H_4O^+$)[25] was detected only when pVI or pAA, respectively, was deposited on the Ecoflex-CNT samples to form the g-IPN (Figure S9c and d and Figure S10c and d). Moreover, for the g-IPN, while the intensity of the characteristic fragment ion of Ecoflex-CNT (*i.e.*, Si^+) remained constant throughout the entire depth profile, that of pVI or pAA decreased exponentially from the surface (Figure S9d

and S10d). These results confirm that the g-IPN was formed near the surface in both cases, as intended.

Similar to the g-IPN synthesized using pVP (Figure 2h), preexisting wrinkles were also observed in the g-IPN synthesized using pVI or pAA (Figure S9e and S10e). This indicates the formation of a relatively stiff surface layer tightly bound to the elastomeric substrate. Moreover, the g-IPN synthesized using pVI or pAA did not exhibit delamination even after being released from 100% uniaxial strain, and only small traces of microcracks were observed, indicating characteristics of effective strain delocalization (Figure S9e and S10e). These results suggest that the g-IPN synthesized using pVI or pAA has high interfacial toughness.

To evaluate the triboelectric properties of the Ecoflex-CNT with g-IPN synthesized using pVI or pAA ($t_{\text{IPN,equiv}}$ = 75 nm), 2D-structured TENGs with a contact-separation mode were fabricated (Figure S9f and S10f). For the bottom layers of the 2D-structured TENGs, the Ecoflex-CNT with g-IPN synthesized using pVI or pAA ($t_{\text{IPN,equiv}}$ = 75 nm) and their control groups were prepared. For the control groups, pure Ecoflex-CNT and a pure pVI or a pure pAA film deposited on Au instead of Ecoflex-CNT (each with a thickness of 3 μm) were prepared to evaluate the triboelectric properties of the pure materials comprising the g-IPN. When the g-IPN synthesized using pVI and its control groups were used as the bottom layers, Kapton, ETFE, and PFA films attached to the copper induction electrode were used as the counter-contacting layers. However, when the g-IPN synthesized using pAA and its control groups were used as the bottom layers, Nylon 66, Glass, and PS films attached to the copper induction electrode were used as the counter-contacting layers, because pAA was more tribo-negative than the pure Ecoflex-CNT. The measured Q_{SC} and V_{OC} are plotted in Figure S9g and S10g. The Q_{SC} and V_{OC} of the Ecoflex-CNT with g-IPN were consistently larger than those of the control groups, irrespective of the counter-contacting materials and the guest polymers.

Note S4. Theoretical calculation process of RCA.

The surface of the Ecoflex-CNT with g-IPN varied from soft (surface elastic modulus of several MPa) to stiff (surface elastic modulus of thousands of MPa) as $t_{\text{IPN,equiv}}$ increased. This implies that the RCA between the Ecoflex-CNT with g-IPN and the counter-contacting material (Kapton) may notably change between the two extremes: the high level of RCA between pure Ecoflex-CNT and Kapton, and the low level of RCA between pure pVP and Kapton. Therefore, the Persson theory, known for its accuracy across a wide range of RCA values, was employed to calculate RCA.[21,26–28] In this work, we employed a simple version of the Persson theory which only considered surface roughness and the depth profile of elastic modulus, while neglecting the influence of adhesion, viscoelasticity, and plastic yield. It is worth noting that the purpose of calculating RCA is to roughly estimate the impact of $t_{\text{IPN,equiv}}$ on the output performance of the 2D-IPN-TENG.

To calculate RCA, the effective elastic modulus (E_{eff})[21] and surface roughness power spectral density $(C(q))$[29,30] are required (Figure 4e). Since g-IPN has a depth-directional gradient profile, the elastic modulus is not constant along the depth direction. In this case, E_{eff} should be calculated using equation (1).[21]

$$E_{eff}(\zeta) = q \int_{0}^{\infty} dz E(z) e^{-qz}$$

(1)

Here, ζ, q, and z denote the magnification, wavevector, and depth from the surface of the sample, respectively. Therefore, to obtain E_{eff}, the depth profile of elastic modulus $(E(z))$ is required. However, since $E(z)$ cannot be measured directly, it was indirectly obtained based on the composition of three relations: the calibrated ToF-SIMS depth profile (R1), the relation between surface ToF-SIMS intensity and $t_{\text{IPN,equiv}}$ (R2), and the relation between surface elastic modulus and $t_{\text{IPN,equiv}}$ (R3). First, the relation between surface ToF-SIMS intensity and surface elastic modulus was obtained by the composition of R2 and R3. Then, the relation between surface ToF-SIMS intensity and surface elastic modulus was used to convert R1 into the depth profile of elastic modulus $(E(z))$.

To obtain R1, the depth calibration of the ToF-SIMS depth profile was performed using a method similar to that used in a previous work.[31] Initially, the sputter rates of the pure materials which comprise g-IPN, under 5 keV Ar_{1450}^{+} gas cluster ion beam (GCIB), were experimentally quantified by sputtering pure samples of the pVP and Ecoflex-CNT. The pure

pVP film was deposited on a Si wafer using the iCVD process, and its thickness was directly measured with ellipsometry. From its ToF-SIMS depth profile, the time to completely sputter the pure pVP film was obtained. Based on this sputtering time and the measured thickness of the pure pVP film, the sputter rate of the pure pVP was estimated to be 7.55 nm s^{-1}.

Unlike the pure pVP, pure Ecoflex-CNT could not be deposited as a thin film on any substrate. Therefore, the sputter rate of pure Ecoflex-CNT was estimated by sputtering a bulk sample of pure Ecoflex-CNT for a sufficiently prolonged time. After sputtering the surface of pure Ecoflex-CNT, the height difference between the sputtered area and the intact area was measured using AFM. By dividing this measured height difference by the total sputtering time, the sputter rate of the pure Ecoflex-CNT was estimated to be 0.08 nm s^{-1}.

In the case of g-IPN, because of its depth-directional gradient profile, the sputter rate may vary with the depth-dependent concentration of pVP and Ecoflex-CNT. Therefore, the depth-dependent sputter rate of g-IPN, at a single data point in a ToF-SIMS depth profile, was assumed to be the sum of the sputter rates of the pVP and Ecoflex-CNT components, which were assumed to be proportional to their ToF-SIMS intensity.[31] As examples, the calibrated ToF-SIMS depth profiles are shown in Figure S16.

To obtain R2, the ToF-SIMS intensity was measured at the surface of the Ecoflex-CNT with g-IPN. As shown in Figure S17a, the surface intensity of $C_6H_{10}NO^+$ (the characteristic fragment ion of pVP) increased monotonically with increasing $t_{\text{IPN,equiv}}$. It should be noted that the analysis depth for ToF-SIMS measurements without sputtering is normally less than a few nanometers.[32]

To obtain R3, the surface elastic modulus was measured for various $t_{\text{IPN,equiv}}$, using F-d spectroscopy. To obtain the composition of R2 and R3, the analysis depth of the surface ToF-SIMS intensity measurement and the indentation depth for the surface elastic modulus measurement should be as similar as possible. Therefore, the peak force used for measuring the F-d curve, which is the maximum force at which the AFM probe indents the surface of the sample, was set to indent the surface by only 7 nm. Since the surface elastic modulus depends on $t_{\text{IPN,equiv}}$, this peak force was varied with $t_{\text{IPN,equiv}}$. Examples of the measured F-d curves are shown in Figure S17b-d.

From the measured F-d curves, the surface elastic modulus of the Ecoflex-CNT with g-IPN was roughly estimated to range from several MPa (at $t_{\text{IPN,equiv}} = 0$ nm, $i.e.$, pure Ecoflex-

CNT) to thousands of MPa (at $t_{IPN,equiv}$ = 1000 nm, *i.e.*, over-deposited sample). For the accurate extraction of the surface elastic modulus from the *F-d* curve, different contact mechanics models were utilized, depending on the range of surface elastic modulus.[33] Therefore, for $t_{IPN,equiv}$ ranging from 0 nm to 10 nm, the Johnson-Kendall-Roberts (JKR) model was used, and for $t_{IPN,equiv}$ ranging from 25 nm to 1000 nm, the Derjaguin-Muller-Toporov (DMT) model was used.[33] The extracted surface elastic modulus values for various $t_{IPN,equiv}$ are shown in Figure 4f.

By the composition of R1 (Figure S16), R2 (Figure S17a), and R3 (Figure 4f), the depth profile of elastic modulus ($E(z)$) was obtained for various $t_{IPN,equiv}$, as shown in Figure S18. Linear interpolation was used for the composition of R1, R2 and R3. Note that the Persson theory utilizes the concept of magnification (ζ), which describes the length scale of interest.[21] Specifically, ζ is a dimensionless parameter defined as L/λ, where L is the lateral size of a sample, and λ is the shortest wavelength of surface roughness that can be resolved for a given ζ. Although a high ζ is preferred to describe CE occurring at the atomic scale, in our case, too high ζ is meaningless when it exceeds the resolution of the AFM measurements. Therefore, ζ was set to be 512,000, which corresponded to the resolution of our AFM measurements. Using ζ and $E(z)$, E_{eff} was calculated for various $t_{IPN,equiv}$, according to equation (1) (Figure S19a).

As shown in Figure 4e, the RCA calculation also requires the surface roughness power spectral density ($C(q)$).[29,30] The $C(q)$ was measured by multi-scale AFM topography measurements. Specifically, to measure $C(q)$ at large wavevectors, a topography was acquired with a scan size of 5 μm × 5 μm and a resolution of approximately 19.5 nm. For the measurement of $C(q)$ at small wavevectors, a topography was acquired with a scan size of 100 μm × 100 μm and a resolution of approximately 390.63 nm. The resulting $C(q)$ for various $t_{IPN,equiv}$ are shown in Figure S19b. Note that the $C(q)$ of the counter-contacting material (Kapton in this case) is also an important factor in calculating RCA.[26] However, it was not considered in our calculations because the $C(q)$ of Kapton was much lower than that of Ecoflex-CNT with g-IPN.

Finally, the normalized RCA, shown in Figure 4g, was calculated using equations (2), (3), and (4) with the calculated E_{eff} (Figure S19a) and the measured $C(q)$ (Figure S19b).[26,27]

$$\frac{1}{E^*} = \frac{1 - \nu_{Kapton}^2}{E_{Kapton}} + \frac{1 - \nu_{g-IPN}^2}{E_{eff}} \qquad (2)$$

$$G(\zeta) = \frac{\pi}{4}E^{*\,2}\int_{q_L}^{\zeta q_L} dq\, q^3 C(q)$$

(3)

$$\frac{A_R(\zeta)}{A_0} = erf\left(\frac{\sigma_0}{2\sqrt{G}}\right)$$

(4)

In equation (2), E^* is the composite elastic modulus, v_{Kapton} is the Poisson's ratio of Kapton,[34] E_{Kapton} is the elastic modulus of Kapton, and $v_{g\text{-}IPN}$ is the Poisson's ratio of g-IPN (assumed to be 0.5). In equation (3), q_L is the smallest possible wavevector ($2\pi/L$), and L is the lateral size of a sample (2 cm). For equation (4), σ_0 is the nominal pressure (150 kPa), A_R represent the RCA, and A_0 represent the nominal contact area.

Note S5. A simple analytical model describing the increase in surface area of the Ecoflex-CNT with g-IPN ($t_{IPN,equiv}$ = 75 nm) under increasing strain.

When Ecoflex-CNT with g-IPN ($t_{IPN,equiv}$ = 75 nm) was subjected to large strain, unlike the surface of pure Ecoflex-CNT, the stiff surface IPN layer cracked and wrinkled, exposing the underlying intrinsically stretchable IPN layer to the ambient. This increased the surface area of Ecoflex-CNT with g-IPN, thereby preventing the degradation of Q_{SC} and V_{OC} with increasing strain. This is referred to as the strain-compensating ability. Here, to quantitatively explain the increase in surface area with increasing strain, the surface area is modeled analytically using a simple modification of the well-known Poisson effect.[35]

Intrinsically stretchable materials, such as pure Ecoflex-CNT, obey the Poisson effect when they are stretched (*i.e.*, they contract in the direction perpendicular to stretch), as illustrated in Figure S23a. Brittle materials like pVP fracture with only a small amount of strain, as depicted in Figure S23b. Ecoflex-CNT with g-IPN ($t_{IPN,equiv}$ = 75 nm) is a special case where a thin layer of brittle material is tightly bound to the surface of an intrinsically stretchable material. In this case, upon increasing strain, the stiff surface IPN layer cracks along the direction of stretch, exposing the buried intrinsically stretchable IPN layer to the ambient. Simultaneously, the cracked stiff surface IPN layer wrinkles along the direction perpendicular to stretch due to the compressive stress caused by the intrinsically stretchable substrate, as shown in Figure S23c.

The increase in surface area with increasing strain for the Ecoflex-CNT with g-IPN can be predicted by modeling the ratio between the surface area (A_S) and the nominal area (A_N). From Figure S23c, A_N can be expressed using equation (5) according to the Poisson effect, where L_0, W_0, ε, and v denote the initial length of a sample, the initial width of a sample, the strain applied to the sample, and the Poisson's ratio of an intrinsically stretchable substrate, respectively. The A_S of stretched Ecoflex-CNT with g-IPN is the sum of two contributions: one from the cracked and wrinkled stiff surface IPN layer, and the other from the newly exposed intrinsically stretchable IPN layer. The first term in equation (6) describes the surface area of the stiff surface IPN layer, which is assumed to remain invariant with increasing strain due to its relative rigidity. On the other hand, the second term in equation (6) represents the additional surface area provided by the exposure of the intrinsically stretchable IPN layer with increasing strain. Therefore, the ratio of A_S to A_N can be expressed by equation (7). Note that for ideal intrinsically stretchable materials such as pure Ecoflex-CNT, the ratio between A_S and A_N

should be unity, regardless of strain.

$$A_N = L_0 W_0 (1 + \varepsilon)(1 - \nu\varepsilon) \quad (5)$$

$$A_S = L_0 W_0 + L_0 W_0 \varepsilon(1 - \nu\varepsilon) \quad (6)$$

$$\frac{A_S}{A_N} = \frac{1}{(1 + \varepsilon)(1 - \nu\varepsilon)} + \frac{\varepsilon}{1 + \varepsilon} \quad (7)$$

According to equation (7), by assuming a ν of 0.5, the ratio of A_S to A_N rapidly increases with increasing strain, as shown in Figure S23d. This trend is consistent with the surface ToF-SIMS intensity results, especially when the strain exceeded the crack-onset strain (Figure 5g).

It is worth noting that our model assumes the crack-onset strain of the stiff surface IPN layer to be 0%, for the sake of convenience. However, in reality, the crack-onset strain of the stiff surface IPN layer was greater than 0%, and the intrinsically stretchable IPN was not exposed when the strain was below the crack-onset strain (Figure S25). Therefore, our model is not valid when the strain is below the crack-onset strain (Figure 5j).

Note S6. Theoretical and experimental optimization of pore diameter for the sponge-structured 3D elastic TENGs.

The pore diameter of the Ecoflex-CNT sponge (t_{pore}) was optimized to maximize the output energy density of the 3D-TENG. Since the largest possible output energy density (E_{max}) of a 3D-TENG is directly proportional to the product of $Q_{SC,vol}$ and V_{OC},[36] the dependences of $Q_{SC,vol}$ and V_{OC} on t_{pore} were analytically modeled and experimentally measured. Subsequently, the t_{pore} that maximized the product of $Q_{SC,vol}$ and V_{OC} was selected for further experiments on the 3D-TENG and 3D-IPN-TENG.

By assuming the ideal coaxial alignment of a pore and a wire in a single 3D-TENG component (Figure S29a), the $Q_{SC,vol}$ and V_{OC} can be expressed as equations (8) and (9), based on their equivalent circuit. Other structural parameters, such as the thickness of the Ecoflex-CNT wall between adjacent pores (t_{wall}), the diameter of the copper core (t_{Cu}) in a wire, the outer diameter of a wire (t_{wire}), and the length of a wire (l), were fixed at 500 μm, 250 μm, 300 μm, and 2 cm, respectively.

$$Q_{SC,vol} = \frac{1}{l(t_{wall} + t_{pore})^2} \frac{C_{int}}{C_{int} + C_{ext,r}} Q \quad (8)$$

$$V_{OC} = \frac{Q}{C_{ext,r}} \quad (9)$$

$$C_{int} = \frac{2\pi l \varepsilon_0 \varepsilon_{Kapton}}{\ln\left(\dfrac{t_{wire}}{t_{Cu}}\right)} \quad (10)$$

$$C_{ext,r} = \frac{2\pi l \varepsilon_0}{\ln\left(\dfrac{t_{pore}}{t_{wire}}\right)} \quad (11)$$

Here, C_{int} in equation (10) represents the capacitance between the outer surface of a wire and the copper core. $C_{ext,r}$ in equation (11) denotes the capacitance between the outer surface of a wire and the Ecoflex-CNT sponge in the relaxed state. Q, ε_0, and ε_{Kapton} represent the total surface charge on a wire, vacuum permittivity, and dielectric constant of Kapton, respectively.

The modeled $Q_{SC,vol}$, V_{OC}, and their product, according to equations (8) and (9), are shown in Figure S29b. The optimal t_{pore}, predicted from the product of $Q_{SC,vol}$ and V_{OC}, was found to be near 730 μm.

Furthermore, the dependences of $Q_{SC,vol}$ and V_{OC} on t_{pore} were experimentally measured using the fabricated 3D-TENGs with various values of t_{pore}. As shown in Figure S29c, the experimentally measured $Q_{SC,vol}$ and V_{OC} showed trends similar to the theoretical results. The experimentally determined optimal t_{pore} that maximized the product of $Q_{SC,vol}$ and V_{OC} was 600 μm, which was similar to the optimal t_{pore} obtained from the analytical modeling. Therefore, the 3D-TENG and 3D-IPN-TENG with a t_{pore} of 600 μm were used for further experiments.

Supplementary References

1   S. S. Kwak, S. M. Kim, H. Ryu, J. Kim, U. Khan, H.-J. Yoon, Y. H. Jeong and S.-W. Kim, *Energy Environ. Sci.*, 2019, **12**, 3156–3163.

2   K. C. Pradel and N. Fukata, *Nano Energy*, 2021, **83**, 105856.

3   T. Prada, V. Harnchana, A. Lakhonchai, A. Chingsungnoen, P. Poolcharuansin, N. Chanlek, A. Klamchuen, P. Thongbai and V. Amornkitbamrung, *Nano Res.*, 2022, **15**, 272–279.

4   W. Zhang, Q. Liu, S. Chao, R. Liu, X. Cui, Y. Sun, H. Ouyang and Z. Li, *ACS Appl. Mater. Interfaces*, 2021, **13**, 42966–42976.

5   J. Zhao, Y. Xiao, W. Yang, S. Zhang, H. Wang, Q. Wang, Z. Sun, W. Li, M. Gao, Z. Wang, Y. Xu, H. Chen and J. Wang, *Adv. Mater. Technol.*, 2023, **8**, 2201769.

6   H. Li, X. Fang, R. Li, B. Liu, H. Tang, X. Ding, Y. Xie, R. Zhou, G. Zhou and Y. Tang, *Nano Energy*, 2020, **78**, 105288.

7   J. X. Liu, G. Liu, Z. H. Guo, W. Hu, C. Zhang and X. Pu, *Chem. Eng. J.*, 2023, **462**, 142167.

8   H. Chen, Y. Xu, J. Zhang, W. Wu and G. Song, *Nano Energy*, 2019, **58**, 304–311.

9   L. Yang, C. Liu, W. Yuan, C. Meng, A. Dutta, X. Chen, L. Guo, G. Niu and H. Cheng, *Nano Energy*, 2022, **103**, 107807.

10   W. Wu, X. Peng, Y. Xiao, J. Sun, L. Li, Y. Xu, S. Zhang, K. Dong and L. Wang, *Mater. Today Chem.*, 2023, **27**, 101286.

11   S. K. Ghosh, J. Kim, M. P. Kim, S. Na, J. Cho, J. J. Kim and H. Ko, *ACS Nano*, 2022, **16**, 11415–11427.

12   J. Qian, J. He, S. Qian, J. Zhang, X. Niu, X. Fan, C. Wang, X. Hou, J. Mu, W. Geng and X. Chou, *Adv. Funct. Mater.*, 2020, **30**, 1907414.

13   S. M. S. Rana, M. A. Zahed, M. R. Islam, O. Faruk, H. S. Song, S. H. Jeong and J. Y. Park, *Chem. Eng. J.*, 2023, **473**, 144989.

14   M. Salauddin, S. M. S. Rana, M. Sharifuzzaman, H. S. Song, M. S. Reza, S. H. Jeong and J. Y. Park, *Adv. Energy Mater.*, 2023, **13**, 2203812.

15   D. W. Kim, J. H. Lee, I. You, J. K. Kim and U. Jeong, *Nano Energy*, 2018, **50**, 192–200.

16   J. Kang, J. Mun, Y. Zheng, M. Koizumi, N. Matsuhisa, H.-C. Wu, S. Chen, J. B.-H. Tok, G. H. Lee, L. Jin and Z. Bao, *Nat. Nanotechnol.*, 2022, **17**, 1265–1271.

17   A. Hillerström and B. Kronberg, *J. Appl. Polym. Sci.*, 2008, **110**, 3059-3067.

18   A. Hillerström, M. Andersson, J. S. Pedersen, A. Altskär, M. Langton, J. van Stam and B. Kronberg, *J. Appl. Polym. Sci.*, 2009, **114**, 1828-1839.

19   H.-R. Lim, Y.-S. Kim, S. Kwon, M. Mahmood, Y.-T. Kwon, Y. Lee, S. M. Lee and W.-H. Yeo, *Sensors*, 2020, **20**, 3297.

20   T. H. Lee and J. Y. Jho, *Macromol. Res.*, 2018, **26**, 659–664.

21   B. N. J. Persson, *Surf. Sci. Rep.*, 2006, **61**, 201–227.

22   G. Min, Y. Xu, P. Cochran, N. Gadegaard, D. M. Mulvihill and R. Dahiya, *Nano Energy*, 2021, **83**, 105829.

23   Y. Xu, G. Min, N. Gadegaard, R. Dahiya and D. M. Mulvihill, *Nano Energy*, 2020, **76**, 105067.

24   M. Dahlström, P. R. Jonsson, J. Lausmaa, T. Arnebrant, M. Sjögren, K. Holmberg, L. G. E. Mårtensson and H. Elwing, *Biotechnol. Bioeng.*, 2004, **86**, 1-8.

25   G. J. S. Fowler, G. Mishra, C. D. Easton and S. L. McArthur, *Polymer*, 2009, **50**, 5076-5083.

26   C. Yang and B. N. J. Persson, *J. Phys.: Condens. Matter*, 2008, **20**, 215214.

27   B. N. J. Persson, O. Albohr, U. Tartaglino, A. I. Volokitin and E. Tosatti, *J. Phys.: Condens. Matter*, 2005, **17**, R1.

28   B. N. J. Persson, *Phys. Rev. Lett.*, 2001, **87**, 116101.

29   T. D. B. Jacobs, T. Junge and L. Pastewka, *Surf. Topogr.: Metrol. Prop.*, 2017, **5**, 013001.

30   M. C. Röttger, A. Sanner, L. A. Thimons, T. Junge, A. Gujrati, J. M. Monti, W. G. Nöhring, T. D. B. Jacobs and L. Pastewka, *Surf. Topogr.: Metrol. Prop.*, 2022, **10**, 035032.

31   K. Jeong, Y. Lee, Y. Kim, H. Mun, K.-U. Kyung and S. G. Im, *Chem. Eng. J.*, 2022, **429**,

132250.

32   T. J. Barnes, I. M. Kempson and C. A. Prestidge, *Int. J. Pharm.*, 2011, **417**, 61–69.

33   S. Kim, Y. Lee, M. Lee, S. An and S.-J. Cho, *Nanomaterials*, 2021, **11**, 1593.

34   C. L. Bauer and R. J. Farris, *Polym. Eng. Sci.*, 1989, **29**, 1107-1110.

35   Y. Yang, J. Han, J. Huang, J. Sun, Z. L. Wang, S. Seo and Q. Sun, *Adv. Funct. Mater.*, 2020, **30**, 1909652.

36   Y. Zi, J. Wang, S. Wang, S. Li, Z. Wen, H. Guo and Z. L. Wang, *Nat. Commun.*, 2016, **7**, 10987.